IMPACT OF REDUCTION-OXIDATION AGENTS ON THE HIGH TEMPERATURE CORROSION OF MATERIALS IN LIF-NAF-KF

BY ROBERT STEVEN SELLERS

THESIS

Submitted in partial fulfillment of the requirements for the degree of

MASTER OF SCIENCE

(MECHANICAL ENGINEERING)

at the

UNIVERSITY OF WISCONSIN-MADISON

2012

Advisor Approval

Impact of Reduction-Oxidation Agents on the High Temperature Corrosion of Materials in LiF-NaF-KF

by Robert Steven Sellers

Thesis
Submitted in partial fulfillment of the requirements for the degree of
Master of Science
(Mechanical Engineering)
at the
University of Wisconsin-Madison
August, 2012

Thesis approved by:

Chair of Committee: Dr. Todd R. Allen _____
(Advisor Signature)

Committee Members: Dr. Mark H. Anderson _____

Dr. Kumar Sridharan _____

Dr. Michael L. Corradini _____

Acknowledgements

Thank you to Dr. Mark Anderson and Dr. Kumar Sridharan for providing insight, instruction, and thesis advice.

Thank you to Professor Todd Allen and Professor Michael Corradini for guidance and serving on the thesis defense committee.

Thank you to Paul Brooks and Ben Linkert for machine shop assistance, welding, and advice.

Thank you to the graduate students who assisted in various aspects of this research project: Brian Kelleher, Sean Martin, Wei-Jen Cheng, James Ambrosek, Paul Weber, and Guiqiu Zheng.

Table of Contents

List of Figures

List of Tables

1 Abstract

Molten FLiNaK salt (LiF-NaF-KF: 46.5-11.5-42 mol %) has been proposed for use as secondary reactor coolants, media for transfer of high temperature process heat from nuclear reactors to chemical plants, and for concentrated solar power thermal energy storage. By using molten salts as thermal exchange media, an increase in power conversion efficiency can be achieved through use of a high temperature power conversion process. However, at proposed high temperature operating temperatures, material compatibility and corrosion issues present an engineering challenge. Previous studies at the University of Wisconsin-Madison have focused on exposing a variety of high temperature alloys to the same molten salt conditions. The scope of this study is narrowed towards exposing 316L stainless steel and Hastelloy-N to a variety of molten salt chemistry conditions. Baseline corrosion rates were studied through exposing only the test materials to molten FLiNaK salt at 850°C for 1000 hours in a stainless steel crucible. 316L stainless steel experienced classic molten salt corrosion through near surface depletion of chromium, while corrosion products derived from the stainless steel crucible electroplated to the nickel based Hastelloy-N. To identify transient corrosion effects, several crucibles were tested for 2000 hours. No significant corrosion was observed due to an increase in exposure time.

Besides examining baseline corrosion characteristics, an experimental basis is established for controlling corrosion through the addition of metallic zirconium or sodium as a reduction-oxidation (redox) agent. It is theorized that a redox agent placed in a molten salt environment will enforce a reducing environment within the salt and, by extension, reduce attack on chromium. Zirconium and sodium appear to successfully diminish attack on chromium, however, quantity of redox agent in the system is an important consideration.

Many next generation nuclear reactor designs rely on large quantities of graphite for its advantageous properties in a nuclear environment, and previous work has shown that graphite can influence corrosion characteristics of fluoride salts. A secondary goal of this work is to further investigate these accelerated corrosion effects as well as identify any new interactions between graphite and redox agents in a molten salt environment.

2 Background

2.1 Past and Present Molten Fluoride Salt Nuclear Research Initiatives in the US

Molten fluoride salts for nuclear applications have a rich history in the United States. During the Cold War, the United States began the Aircraft Reactor Experiment (ARE) with the goal of building a nuclear powered aircraft which could achieve sustained flight without refueling. To achieve the power density required to make the concept viable, engineers devised a system where fissile nuclear fuel was dissolved into a molten fluoride salt mixture, eliminating the need for solid metal fuel and cladding. During the ARE, a Ni-Mo-Cr alloy was developed for the purpose of resisting fluoride corrosion while maintaining high temperature strength [1]. The alloy in its current form is trademarked Hastelloy-N, and is owned by Haynes International [2]. In 1954, the Aircraft Reactor Experiment was successfully run for nine consecutive days at hot leg temperatures up to 860°C and powers up to 2.5 MW_t [3]. Though the Aircraft Reactor Experiment was eventually ended, some results were deemed promising enough to justify further investment for civilian power applications. Construction began in 1962 on the Molten Salt Reactor Experiment (MSRE), a ground based civilian research scale nuclear reactor which relied on molten LiF-BeF2 containing dissolved fissile fluoride salts. Interestingly, a LiF-BeF_2 mixture closer to 66-33mol% was used instead of the eutectic mixture 50-50mol% because the melting

point was higher than the uranium fluoride salt and a lower BeF_2 concentration made for a more advantageous viscosity [4, 5]. The MSRE project ran until 1969 and was critical without incident for 15,424 hours while maintaining hot leg temperatures of 650°C. The MSRE demonstrated the practicality and stability of dissolved fuel circulating molten salt and that corrosion issues could be overcome. Despite the success of the MSRE, funding was diverted in 1976 to the more senior and operationally promising liquid metal breeder reactor program [6, 7].

Table 1. Thermo physical properties of FLiNaK compared with common nuclear heat transport fluids [8]**.**

Fluid	T_m (ºC)	ρ (g/cm^3)	ρ*Cp* (J/cm^3 ºC)	μ (Pa s)	*k* (W/m-K)
LiF-NaF-KF (46.5-11.5-42 mol%), 700ºC	454	2.02	3.8	0.0029	0.92
LiF-BeF2 (66-33 mol%), 700ºC	460	1.94	4.68	0.0056	1
He (7.5MPa)	-	0.0038	0.00209	4.2E-05	0.29
Na	98	0.82	1.01	0.00023	62
H_2O	0	1	4.18	0.001	0.6

2.2 Current Research Initiatives

Interest in molten fluoride salt technologies for nuclear applications has seen a revival in the United States over the past decade due in part to their advantageous thermo physical properties compared to water or pressurized helium, characterized by high thermal conductivity, high specific heat, and broad usable temperature range at atmospheric pressure (Table 1). Generation IV (Gen. IV) nuclear initiatives have selected molten fluoride salts as potential reactor coolants for transfer of high temperature process heat for hydrogen and other chemical production plants [9-11]. In addition to DOE National Laboratory research efforts, collaboration

between three universities (Massachusetts Institute of Technology, University of California-Berkeley, and University of Wisconsin-Madison) has recently begun to renew interest and update molten salt reactor technology. The integrated research project, named Fluoride Salt Cooled High Temperature Reactor (FHR), is funded through the Nuclear Energy University Program (NEUP) with the end goal of creating a pre-conceptual reactor design and development roadmap [11]. The eutectic fluoride salt mixture 46.5%LiF-11.5%NaF-42%KF (mol%), commonly referred to as FLiNaK, is emerging as a leading candidate for use as a secondary heat transfer fluid in Gen. IV and FHR.

However, at the high operational temperatures planned in Gen. IV and FHR initiatives, materials corrosion presents an engineering challenge due to the reduction-oxidation (redox) reaction of fluorine ions with surface protective oxide scales of Cr, Al or Si. In molten fluoride salts, these oxide scales are chemically unstable. Thus, the passivating properties typically exhibited by heat-resistant alloys are rendered ineffective. Although the MSRE successfully operated without substantial alloy corrosion due to the use of Ni-Mo-Cr Hastelloy-N alloy and novel active chemistry control techniques [7, 12, 13], for cost and strength requirements a broader range of fluoride salt compatible alloys needs to be shown to work under different chemistry scenarios at temperatures 100-200°C higher than the MSRE hot leg temperature. Supplementary materials, such as nuclear grade graphite, small quantities of redox metals, or the use of dissimilar alloys in the same molten salt system are common features of Gen. IV and FHR reactor designs and have been shown to impact corrosion behavior of molten fluoride salts [11, 14-16]. The University of Wisconsin-Madison has been tasked with investigating structural alloy corrosion and the impact of additional nuclear materials on corrosion behavior in fluoride salt systems. This present work seeks to establish a basis for explaining these tasks in molten LiF-

NaF-KF eutectic salt through an experimental study of candidate alloy compatibility and material interaction behaviors.

2.3 Previous FLiNaK work at UW Madison

This work serves to expand on the foundational material and thermal hydraulic studies performed in the past several years at the University of Wisconsin-Madison with FLiNaK salt. The first round of corrosion studies performed at the UW consisted of exposing a breadth of high temperature alloys to FLiNaK salt at 850°C. The extent of corrosion was found to roughly correlate to the chromium content of the alloys, whereby high chromium containing alloys experienced higher attack in FLiNaK salt. Pure nickel was shown to resist corrosion the best. Corrosion was also shown to be strongly dependent on material interactions. The impact of two different crucible construction materials (graphite and Incoloy 800H) on the corrosion of Incoloy 800H was examined. Under the same testing conditions, area specific weight loss of the Incoloy 800H sample exposed to FLiNaK salt was approximately 180 times as great when tested in a graphite crucible than the Incoloy 800H crucible. Finally, corrosion characteristics of FLiNaK procured through several sources was compared and shown to produce uniform corrosion results [16-18]. Complementary work was also completed in developing and characterizing protective nickel plating techniques for high chromium alloys. The nickel plating layer was shown to be effective in reducing the diffusion of vulnerable species (Cr, Fe) from the substrate into the FLiNaK bath. However, the plating layer may not be mechanically stable as void formations were observed [19].

Thermal hydraulic forced convection studies have been performed in molten FLiNaK circulation loops dating back to the 1950's through the 1980's and a cumulative literature review was collected by Ambrosek at UW in 2009 [20]. Of note was the wide discrepancy in measured

molten salt thermal conductivity taken from literature. Ambrosek recalculated a number of literature heat transfer coefficients using the same thermal conductivities, and found the values in agreement with the Dittus-Boetler correlation within 15%. However, it was noticed that the data obtained from literature using a nickel based Inconel alloy varied greatly from data collected using 316 stainless steel tubes. It was speculated that corrosion product radiation effects may be the source of the discrepancy, whereby alloy-dependant chromium dissolution into the salt may affect the radiative absorption coefficient. As a part of his dissertation research, Ambrosek constructed a forced convection molten salt loop. Currently, this loop has only measured chloride salt heat transfer coefficients but studies in fluoride salts are planned [21]. Some work has been started at UW-Madison to investigate how the UV-visible spectral properties of molten FLiNaK change with corrosion product concentration. It can be seen that understanding the corrosive properties of molten salts has far reaching impact beyond knowing which alloy is best for which purpose. Furthering the understanding of molten salt corrosion will also benefit the study of molten salt heat transfer and physical property measurement.

2.4 Corrosion in Molten Fluoride Salts

2.4.1 Reduction-Oxidation Potential in Molten Fluoride Salts

Corrosion is the gradual degradation of materials (typically metals) in an oxidizing environment. The reduction-oxidation potential is the tendency to which one species in the system loses electrons (oxidation) and the other species gains electrons (reduction). This tendency, quantified by the thermodynamic constant of reaction, $K = \exp(-\Delta G / RT)$, allows for ranking corrosion reactions according to the Gibbs free energy of formation, or ΔG. Those compounds with a more negative ΔG are more stable. Comparing ΔG of fluoride compounds provides us with a ranking of how thermodynamically favored a particular reaction is, however,

this ranking is a more of a qualitative ranking of the likeliness of reaction [12]. To address corrosion quantitatively, the deviation from thermodynamically ideal behavior would need to be known for each element in the molten salt environment. This quantity is known as the element activity coefficient and is a strong function of the molten salt system (such as crucible material, impurities) and must be determined experimentally [12]. Measurement of element activity coefficient is beyond the scope of this work.

LiF, NaF, and KF do not have any higher or lower oxidation states, so can only be reduced to their respective metals. The ΔG free energy of formation for LiF, NaF, and KF is more negative than typical corrosion products so the reduction-oxidation potential within the salt should not allow for any corrosion to occur, yet molten salts are known historically to be corrosive environments. Contaminants in the salts are known to cause corrosion issues, where impurities such as HF, FeF_2, NiF_2 act as oxidants [12]. Such reactions lead to the oxidation of alloying constituents that form more stable fluoride compounds (more negative Gibbs free energy of formation, ΔG), usually chromium. Such a reaction is shown as:

$$Cr + NiF_2 \leftrightarrow CrF_2 + Ni \qquad (1)$$

In addition, moisture is a large source of impurities in molten salts which have an impact on corrosion characteristics. H_2O is the most common contaminant in FLiNaK due to the hygroscopic nature of one of its constituents, KF. Measurements of the water content of FLiNaK produced in a regular laboratory environment are shown to be as high as 16 wt% [22, 23]. H_2O induced corrosion includes the following reactions; HF generation (Eq. 1-2) and corrosion of metal by HF (Eq. 3) [17, 22].

$$H_2O + 2F^- \leftrightarrow O^{2-} + 2HF \qquad (2)$$

$$H_2O + F^- \leftrightarrow OH^- + HF \qquad (3)$$

$$M^0 + xHF \leftrightarrow x/2H_2 + MF_x \quad (4)$$

Where M = Ni, Fe, Cr etc.

It has been shown that common structural alloying elements used in Fe and Ni based alloys have a propensity to be corroded in molten fluoride salts in the following order: W, Mo, Ni, Co, Fe, Nb, Cr, Mn, Ti, Zr, Al, with Al being the most prone to attack and tungsten being the most noble [16, 24]. Chromium is one of the most vulnerable elements on the list in addition to one of the most widely used alloying constituent in high temperature alloys, therefore, much attention has been directed to the study of chromium attack and movement in salt systems. It has been observed in past molten fluoride static tests that the corrosion rate of different alloys correlates to the percent Cr composition, in which corrosion rate of alloys increased as the Cr content increased [16, 17]. Of all common alloying constituents used in substantial quantities, nickel is the least prone to attack in a fluorinating environment. In the context of a fluoride salt environment, nickel is considered noble and will be referred to as such.

Corrosion products have been shown to be soluble in molten salt environments [25-27]. This behavior is contrary to the passivating characteristic of high temperature alloys, where a thin layer of immobile chrome oxide prevents further diffusion of chromium out of the alloy matrix. Preventing the movement of chromium becomes the focus of structural alloy corrosion reduction in molten salt systems, and is accomplished through limiting the diffusion of chromium out of the alloy, or adjusting the reduction/oxidation potential of the salt into a reducing tendency in order to decrease attack on structural alloys.

2.4.2 Galvanic Corrosion

Galvanic corrosion occurs when metals with differing electromotive potentials (EMP) are immersed in the same electrolyte bath, as in a molten fluoride salt. In a galvanic couple, metal

with more negative EMP tends to act as an anode while metal with more positive EMP tends to act as a cathode. Thus, material corrosion in molten fluoride salts is accelerated due to the oxidation reaction occurring at the anodic metal [17, 22]. This effect can have negative consequences when differing materials are present in the same molten salt system. Electrochemical plating can occur where the corrosion products of one material migrates and plates to the surface of the more cathoidic material. From the ranking measured by Mellors, shown in Table 8, it can be seen that nickel is the most electropositive of common alloying constituents, so it can be expected that alloys with high nickel content will act in cathodically in electrolytic environments containing electronegative elements like zirconium or chromium [28].

2.4.3 Temperature Gradients

Although equilibrium dissolved chromium concentrations have not been measured in coolant salts such as FLiNaK, solubility limits have been shown to vary with temperature in fuel salts like FLiBe [12]. A polythermal molten salt system may have a temperature gradient large enough to cause a significant difference in corrosion product solubility such that species are dissolved in the hot sections and precipitate from the solution in the cold section, plating out onto heat exchanger surfaces. Such a system may never achieve an equilibrium concentration of corrosion products, as the cold freshly diminished molten salt will return to the hot leg where more corrosion products are absorbed as fast as material diffusion rates can allow [29]. Examination of polythermal systems is beyond the scope of this work.

2.5 Reducing Corrosion in Molten Fluoride Salts

2.5.1 Passive and Active Methods

Corrosion reduction techniques generally fall into two categories: passive and active. In passive protection, damage to the molten salt system is prevented by mechanically separating the molten salt from the vulnerable material through the use of noble alloys like Ni-201 or pure nickel coatings. Development of passive nickel coatings for corrosion prevention in FLiNaK at UW-Madison are described by Olson [17, 19]. However, it is not practical to rely only on a passive system because the general ability and aggressiveness of molten salts to corrode is preserved. Moreover, a practical molten salt system cannot feasibly be constructed from noble material due to cost or strength restrictions.

Active systems seek to directly influence the reactions that govern corrosion through the use of molten salt chemistry control systems and corrosion resistant structural alloys. Numerous active corrosion control systems have been employed with success. The ARE and MSRE saw the creation and fine-tuning of what is now called Hastelloy-N; a Ni-Mo-Cr alloy specially created to resist corrosion in molten fluoride salts [30-33]. The alloy relies on a high concentration of nickel and molybdenum, both of which provide excellent resistance to molten salt corrosion [34]. Chromium content has been kept low in Hastelloy-N, which has been shown to be beneficial to molten salt corrosion resistance in conjunction with a high nickel matrix [8]. However, chromium is kept at a high enough level to preserve hot air oxidation resistance [2]. Corrosion of Hastelloy-N in hot molten fluoride salt exposure has been studied in abundance [25, 27, 33, 35-39]. Despite the wealth of corrosion literature pertaining Hastelloy-N corrosion, little is known about corrosion behavior at temperatures upwards of 250°C greater than the data collected during the 1950's through the 1970's.

Another important active corrosion chemistry control technique developed during the ARE and MSRE projects is batch purification. While making a new batch of salt, specially selected gasses were bubbled through the mixture in order to remove unwanted moisture or metallic impurities. A sparge mixture of hydrofluoric acid (HF) and hydrogen (H_2) was found to be optimal in eliminating salt impurities while not inadvertently damaging the salt containment vessel. Following HF/H2 treatment, impurities in the melt were either vaporized out of the mixture or the precipitates mechanically filtered. [40, 41]. In more recent studies, a HF-H2 sparge has been shown to reduce the corrosive effects of molten salts [15] also at an ORNL/Inconel loop [42]. Reducing sulfur concentrations was also important to maintain the integrity of the structural alloys [40, 43].

Arguably the most important system used to control the fluorine redox potential within molten FLiBe during the molten salt reactor experiment relied on a fissile uranium redox couple. Scientists were able to control the ratio of U^{4+}/U^{3+} to about 100:1 in order to favor a reducing potential within the fluoride salt melt. The buffering capacity of this redox couple allowed the melt to maintain a steady reducing environment [44, 45].

2.5.2 Metallic Reducing Agent

A large portion of this present work is focused on an active corrosion reduction technique that requires the introduction of a metallic reducing agent into the molten fluoride salt mixture in order to affect the fluorine reduction-oxidation (redox) potential. In conjunction with other active corrosion methods, the use of a metallic reducing agent has been shown to be an effective technique to restrain the corrosion of materials in molten salt systems [14, 40, 46, 47].

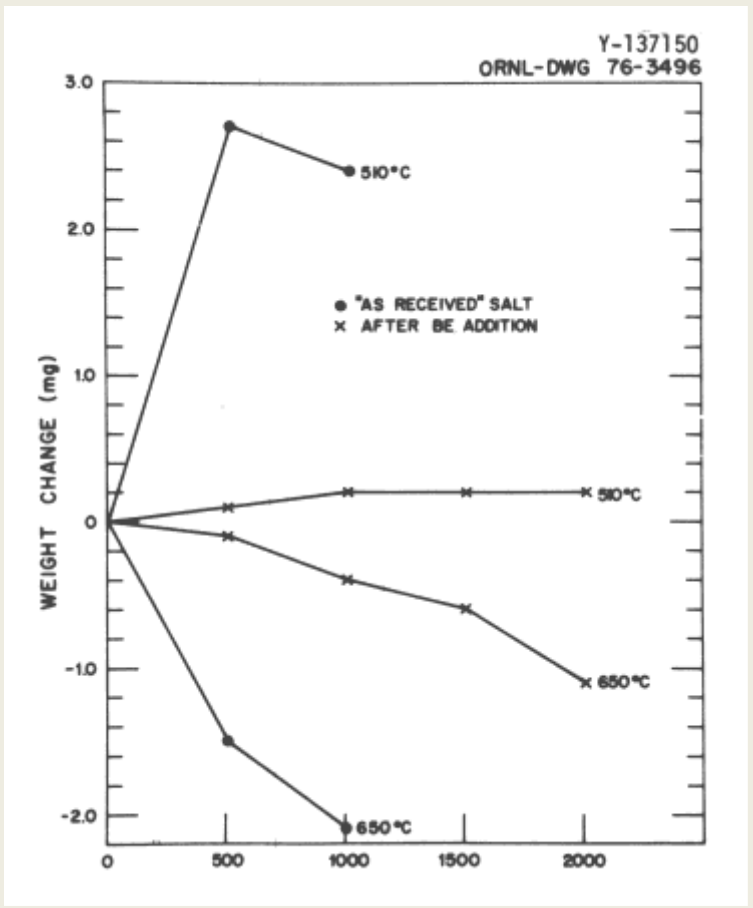

Figure 1. Effect of the addition of a redox agent on weight loss characteristics in molten FLiBe [37]**.**

The purpose of the metallic redox agent is to place the salt system in a reducing state, such that some dissolved fluoride compounds and impurities will be reduced to metal and precipitate out of the molten salt. Figure 1, taken from an early Oak Ridge National Laboratory report, shows the effect of metallic beryllium addition to the corrosivity of molten FLiBe. When Be is present the salt is forced into a reduced state, causing impurities to precipitate from the system which nearly eliminates corrosion at low temperatures. Eliminating impurities has the effect of cleaning the salt and thus decreasing its corrosive potential. To select an appropriate reducing agent, the fluorine compound Gibbs free energy of formation must be taken into account and a metal must be selected so that the resulting redox metal fluorine compound is

more stable than the corrosion products of the molten salt container. In the present work, two metals are selected that meet this criterion: zirconium and sodium. Both exhibit a delta G more negative than chromium, iron, or nickel fluorine compounds.

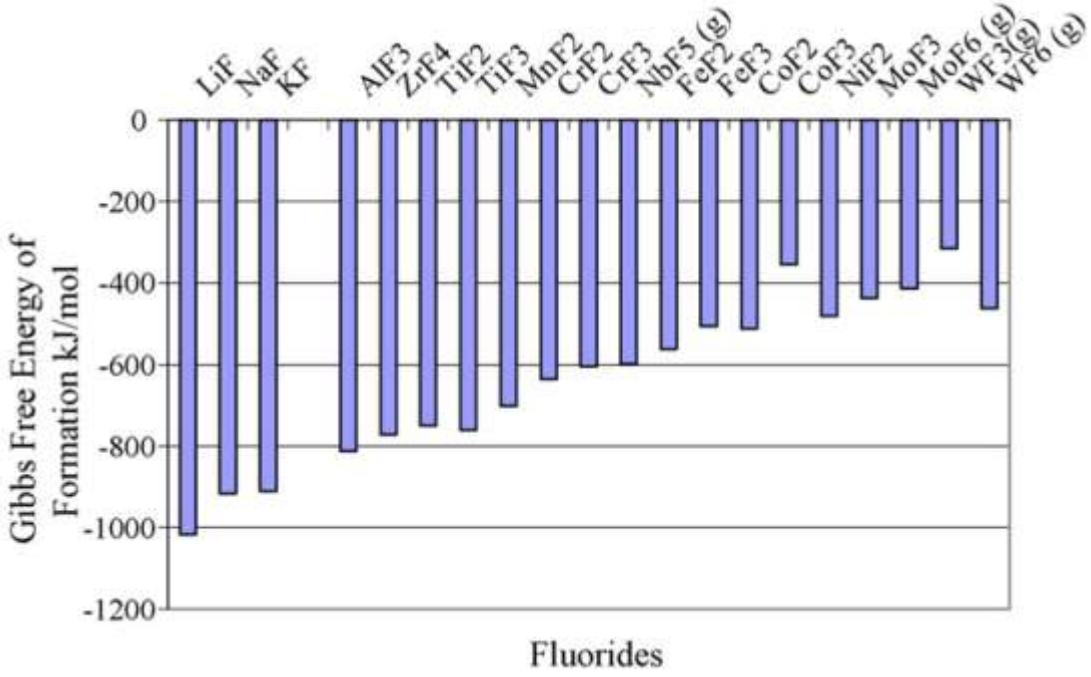

Figure 2. Ranking of the Gibbs Free Energy of Formation for common corrosion products in a molten fluoride salt system [16]**.**

In a realistic molten salt heat exchanger or reactor system there are numerous materials present such as alloys, molten salts, redox agent and graphite which can exhibit unpredictable behaviors when placed in the same system. Therefore, it is pertinent to identify interactions between relevant materials in a practical molten salt system.

3 Experimental

3.1 Static Corrosion Test Overview

Static immersion corrosion tests are a common method for quickly and easily establishing a relative baseline alloy effectiveness comparison in a corrosive medium. Opposed to a dynamic (or flowing) corrosion test, static tests are cheaper and can be quickly fabricated and executed because they don't rely on complicated components like pumps or lengthy trace heat, both of which become problematic at high temperatures. A static test typically only needs four basic components: (1) a static test crucible, (2) the corrosive medium – in this case FLiNaK, (3) the corrosion target material, and (4) a source of heat. There are no officially recognized standards for static immersion corrosion testing, merely guidelines pertaining to material preparation and testing parameters. Instead, components are designed to simulate the intended application of the corrosive medium and target material. According to the ASTM International *Standard Practice for Laboratory Immersion Corrosion Testing of Metal*, "Corrosion testing by its very nature precludes complete standardization" [48].

Due to the necessarily small scale of static corrosion tests, there are emergent corrosion effects which cannot be adequately studied in this form factor, including: galvanic effects created by large disparities in differing material surface area ratios, thermal gradient effects, and flow assisted corrosion effects. Nevertheless, the static corrosion tests in this present work were designed and carried out with immersion testing suggestions of ASTM International, NACE International and ASM International in mind [48-50].

3.2 Materials

3.2.1 Description of FLiNaK Salt

Molten LiF-NaF-KF salt has been proposed for use as secondary reactor coolants, media for transfer of high temperature process heat from nuclear reactors to chemical plants, and for concentrated solar power thermal energy storage [9]. The eutectic fluoride salt mixture, LiF-NaF-KF: 46.5-11.5-42 mol %, commonly referred to as FLiNaK, is emerging as a leading candidate for use as a secondary heat transfer fluid due to its advantageous thermo physical properties compared to water or pressurized helium, characterized by high thermal conductivity, high specific heat, low viscosity, and high boiling point (Table 1).

3.2.2 FLiNaK Production

The FLiNaK used for in this present work was produced in UW-Madison facilities from source components. Previous work performed at UW-Madison compared the corrosion characteristics of FLiNaK from several sources, including highly purified commercial mixtures and mixtures produced in house. No substantial difference in corrosion behavior was found [17]. Source components were procured from Alfa-Aesar and Noah Technology. All components were rated to at least 98.5% purity, with the actual assay much higher (typically 99.5% purity or higher). All components, upon arrival at the university, were immediately stored in dry argon glove box. Following production the FLiNaK salt underwent no additional purification processes.

Figure 3. Argon glove box facilities at the University of Wisconsin-Madison.

The components were combined in the correct ratios under an anhydrous argon atmosphere glove box (Figure 3) and slowly brought up to 700 ^{o}C over five days in a silicon carbide coated graphite crucible to form a homogeneous melt. Each FLiNaK batch was produced in 5kg billets. Individual powders were added in 3 sets of alternating layers for the purpose of creating a more homogeneous melt due to the risk associated with stirring the salt while at high temperatures. All weight measurements were made with an Adventurer Pro scale by Ohaus with a lower limit of +/- .05g. Taking into consideration uncertainties associated with measuring powders (spillage, scale accuracy), a 5kg FLiNaK batch was accurate to within +/- 15g.

After cooling for several days, the solidified salt billet was removed from the production crucible. This billet was then broken up by hand in the glove box to form smaller chunks convenient for loading into a static test crucible. The large billet was broken into smaller pieces, each with a volume of approximately one cubic inch, using a stainless steel chisel and hammer. Previous tests relied on a hot, active transfer system, where salt was moved in liquid form from a

heated container to a heated crucible [16, 17], but it was determined that using a cold technique would be suitable and allow for greater control over the quantity of salt placed in the crucible.

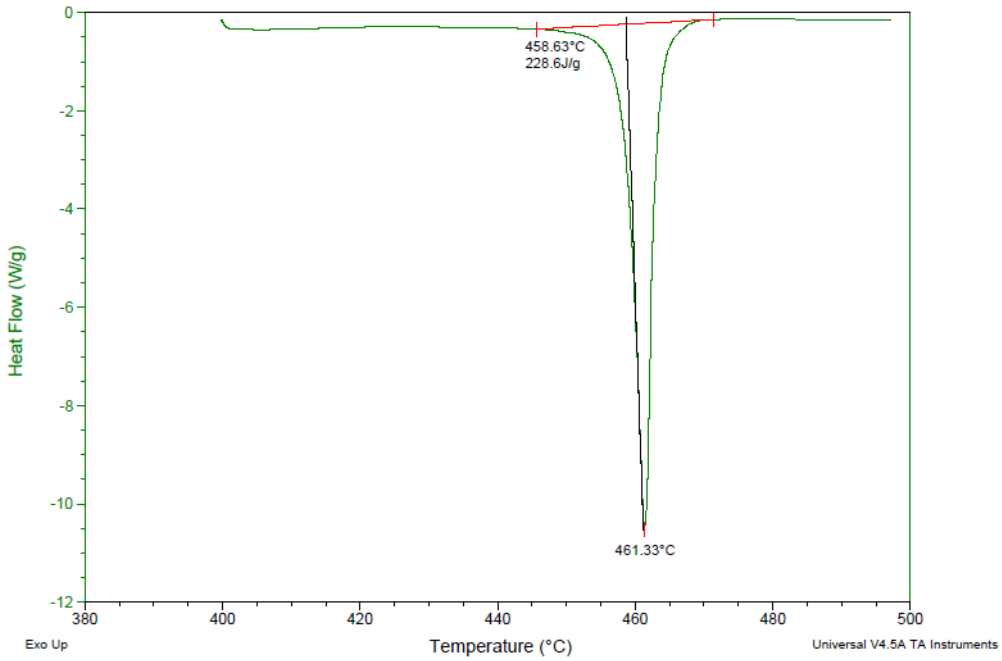

Figure 4. DSC melting point measurement of FLiNaK produced at the University of Wisconsin-Madison.

As an additional way to insure a homogeneous melt, a differential scanning calorimeter (DSC) study was performed on the batches of FLiNaK salt used in the static corrosion tests (Figure 4). Among several other physical properties, a DSC allows for precise measurement of the melting point of a substance. A further explanation of DSC measurements on molten salts is detailed by Ambrosek [21]. The ternary phase diagram eutectic point is 454°C while UW-Madison DSC melting point measurements ranged from 458°C to 460°C [38]. Published FLiNaK corrosion studies have measured melting points up to 464.5°C [22].

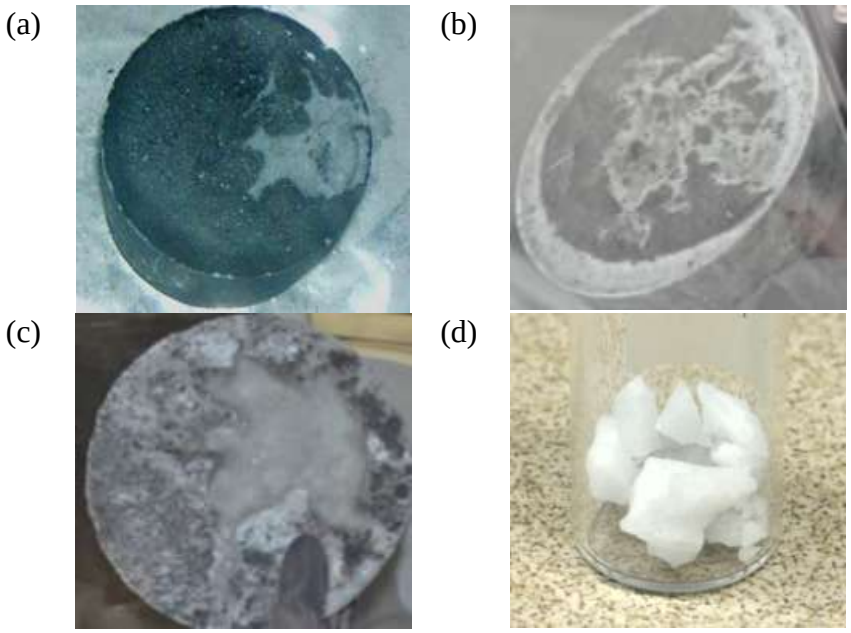

Figure 5. FLiNaK produced at the University of Wisconsin-Madison.

Upon removal from the SiC production crucible, it was noticed that the FLiNaK billet had a thin black coating on the top surface (Figure 5b-c). A similar coating was noticed on FLiNaK produced previously at UW-Madison shown in Figure 5a [17]. Effort was made to identify the black substance using a scanning electron microscope equipped with an energy dispersive x-ray spectrometer (SEM/EDS), however an elemental spectrum different from the FLiNaK components was not identified. The black crust was thin enough that much of it could be removed by hand prior to use in a static corrosion test. Partial removal is shown in Figure 5. Beyond the black layer on the surface, the FLiNaK salt has a white appearance shown in Figure 5. It is suspected that the black crust is carbon accumulation derived from the SiC coated graphite crucible. EDS measurements of carbon is unreliable due to adventitious carbon contamination [51, 52].

Table 2. Chemical composition for 316L and Hastelloy N, weight percent.

Element	C	Fe	Ni	Cr	Mo	Mn	Si	Al	N	Cu	P
316L	0.0225	69[a]	10.0	16.8	2.0	1.5	0.31	-	0.051	0.38	0.031
Hastelloy N	0.08*	4.1	70.7[a]	7.3	16.2	0.66	0.76	0.25	-	-	-

* Maximum [a] As balance

3.2.3 316L Stainless Steel

316, 316L, or 316SS is the designation for the second most used grade of Fe-Cr-Ni austenitic stainless steel in industry, known for good corrosion resistance in marine environments. 316L is typically purchased in dual certification form, meaning the alloy satisfies low carbon restrictions along with the strength requirements of the higher carbon form. Lower carbon (<.03%) 316 stainless steel is more widely used because welding sensitization effects are reduced at lower carbon contents [53]. All 316L stainless steel in this present work is the low carbon version. 316L stainless steel has been widely used as components and structural materials in nuclear power plants because of its excellent high-temperature creep strength and it is one of a handful of alloys with a ASME Code III certification, allowing its use in critical nuclear power plant high temperature components and boilers [54]. 316L is cheaper compared with nickel based alloys such as Hastelloy-N and Inconel alloys due to its iron base. Making 316L compatible with molten salts could result in a tremendous saving in upfront structural material capitol costs for research scale or utility scale molten salt nuclear reactors. The 316L used in this test was procured from various sources in the form of 18 gauge sheet or NPS 2.5 Schedule 10 pipe. Chemical certifications included in the shipment are listed in Table 2.

3.2.4 Hastelloy-N

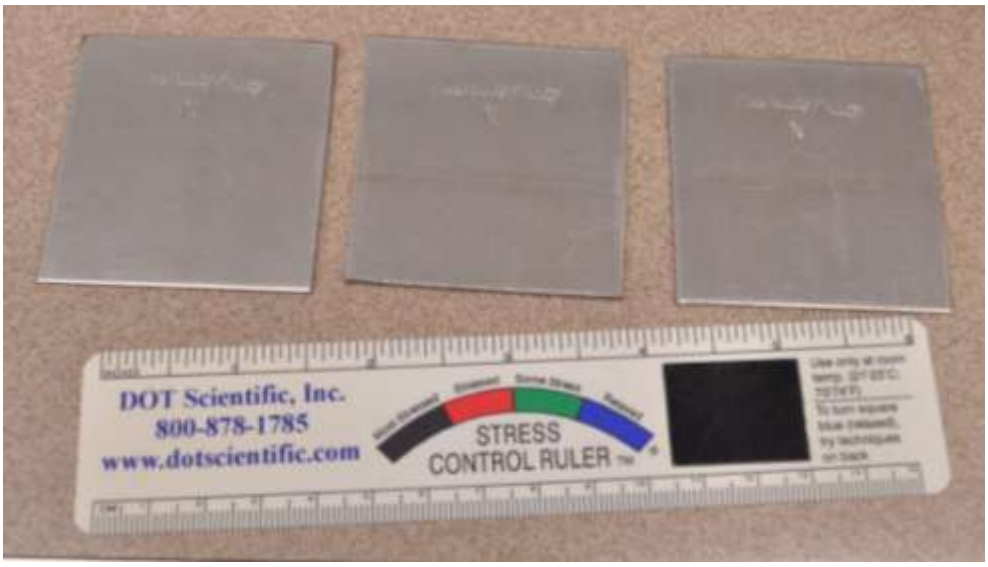

Figure 6. Hastelloy-N coupons received from Haynes International.

Hastelloy-N, on the other hand, is a Ni-Mo-Cr nickel-based alloy developed by Oak Ridge National Laboratory for use in MSRE. Hastelloy-N is a registered trademark of Haynes International. The major Ni and high Mo contents in Hastelloy-N provide the excellent resistance to the molten salt corrosion [30, 34]. Previous studies considering materials corrosion in static molten fluoride salt have shown that alloys with high Ni and low Cr composition can possess better corrosion resistance [8]. Based on this result, Hastelloy-N would have superior resistance to the molten fluoride salt than 316L. As Hastelloy-N is no longer produced, all samples used in testing had to be procured from Haynes International. EDS analysis of the received coupons is shown in Table 2. Hastelloy-N does not have a full high temperature ASME Code III certification.

3.2.5 Redox Agents

Two metallic redox agents are used in this present work. Metallic zirconium was procured from Alfa-Aesar in annealed rod form, 99.92% Hf-excluded purity (1% Hf maximum). Metallic sodium was procured from Alfa-Aesar in ingot form, 99.8% pure (metals basis).

Figure 7. Zirconium ingot used in the static corrosion tests.

Figure 8. Metallic sodium used in the static corrosion tests.

3.3 Static Corrosion Test System

3.3.1 Schematic

A schematic view and corresponding completed crucible can be seen in Figure 9a and Figure 9b. Measurements are in inches unless specified.

(a)

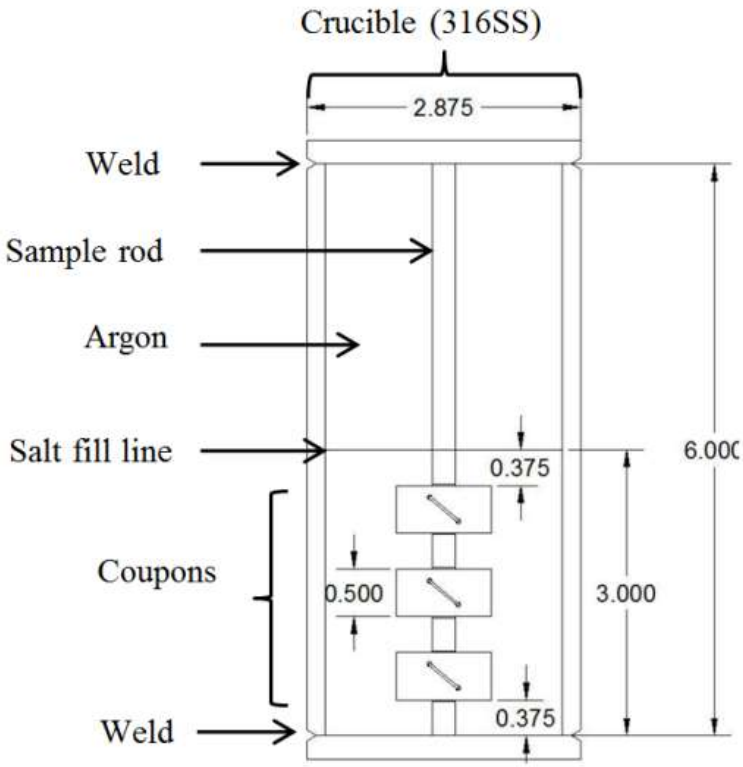

(b)

Figure 9. (a) Schematic view of the static corrosion test crucible. (b) Finished crucible.

3.3.2 Completed Systems

Images of completed crucible systems for test one, two and three are seen in Figure 10, Figure 11, and Figure 12, respectively. Test one and two are identical in design, while test three incorporates the vacuum welding technique for added crucible stability at high temperatures.

Figure 10. Crucibles from test 1 following removal from the furnace after 1000 hours.

Figure 11. Finished crucibles for test 2 prior to heating.

(a)  (b) 

Figure 12. Finished crucibles for test 3 prior to heating. (a) Following argon glove box final welding. (b) Installed in the furnace after vacuum welding.

Figure 13. Crucibles being welded in argon atmosphere glove box.

3.3.3 Materials and Construction

The static corrosion test system is similar in construction to previous UW-Madison static corrosion tests [16, 17, 19, 21, 55]. All crucibles, including end caps and sample mounting rods, were constructed of 316L stainless steel. Test schematic can be seen in Figure 9. Each corrosion system was constructed of a six inch long segment of NPS 2.5, Schedule 10 tube with a 60 degree chamfer on either end. The tubes were cleaned with a boring tool. The end caps were laser cut from ¼ inch 316L sheet. Prior to welding on either end of the six inch length of schedule 10 tubes, the quarter inch tops were faced and chamfered on a lathe. Sample mounting rods were constructed of ¼ inch OD 316L rod. Three shallow grooves were milled into each rod for sample placement. Three corrosion samples per crucible were secured to each sample rod via 316L wire. All crucible components were sequentially cleaned in phosphoric acid and organic solvents to remove fabrication residue.

(a)  (b) 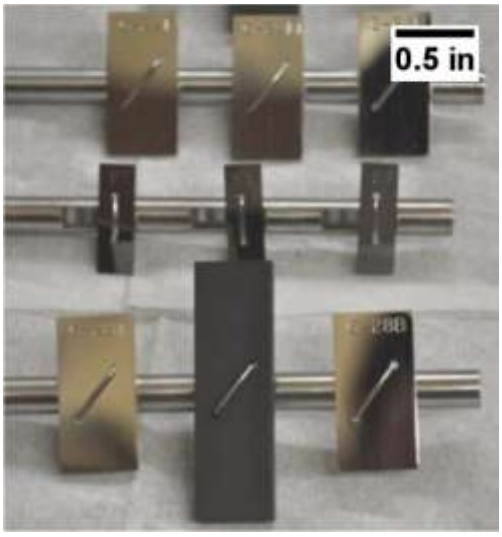

Figure 14. Coupons in various stages of preparation.
(a) Rough 316L prior to polishing and labeling. (b) 316L, Hastelloy-N, and graphite coupons polished, labeled and mounted to the 316L sample rod. The Hastelloy-N samples are kept small to conserve raw materials.

3.3.4 Finishing

In the first two static corrosion tests, all test system components, including crucible, tops, sample rods, and salt, were assembled in room temperature argon atmosphere and then welded shut via ‘cold welding’ method. This technique, while quick, allows for a small quantity of argon to remain inside the crucible indefinitely. The remaining argon content is difficult to calculate, as it depends on the temperature of the crucible which undergoes substantial heating during the two pass welding process. Previous tests used a ‘hot welding’ technique, where the entire crucible was heated during the welding process. The hot welding method allows for greater control over the quantity of remaining argon atmosphere. As the corrosion crucibles are closed systems, any trapped gas will become pressurized during the heating phase. This slight pressurization may lead to unexpected system behaviors and should be avoided. Although the first round static test did not exhibit any adverse reaction to the cold welding method, it is thought that the slight pressurization was a contributing factor to the system failure of the second round corrosion test.

(a)  (b) 

Figure 15. Furnaces used to study the corrosion effects of molten FLiNaK. (a) Inconel furnace with retort. (b) Low cost, high temperature box furnace.

3.3.5 Furnaces

Two different high temperature furnaces were used throughout the three static corrosion tests. Two of the tests were performed in an Inconel furnace with retort seen in Figure 15a. One test was performed in a Sentro Tech ST-1200-161622 high temperature low cost box furnace, shown in Figure 15b. The Inconel furnace proved to be the better option, as it was a more robust construction and the static test crucibles did not exhibit any adverse reactions to the furnace materials. The Sentro Tech box furnace relied on low cost insulation materials and, as a result, is thought to have contributed to the failure of the second round static corrosion system (Appendix A).

3.3.6 Vacuum welding

(a) (b)

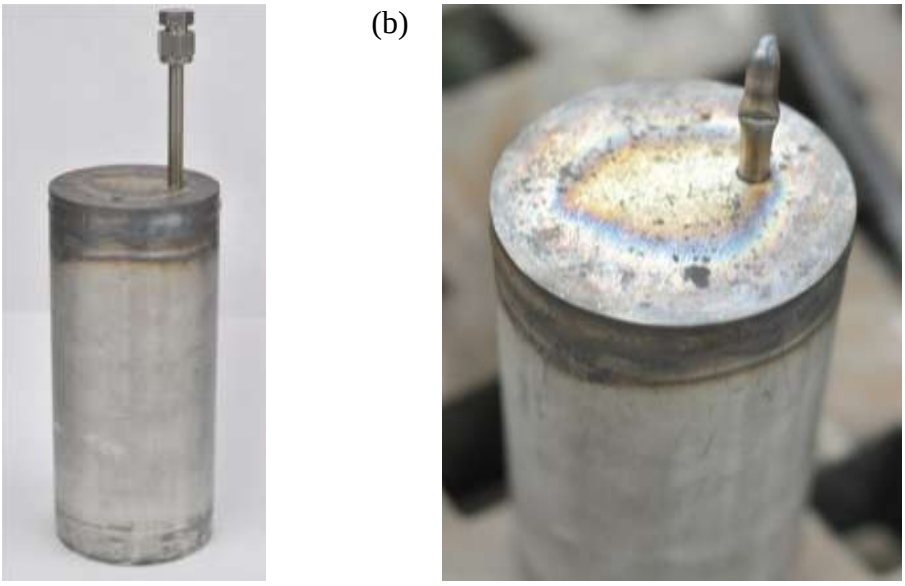

Figure 16. FLiNaK test three vacuum sealed corrosion crucibles. (a) Prior to finishing. (b) Detailed view of vacuum crimp and weld.

As the cold welding technique is suspected to have caused a small internal pressurization contributing to the failure of the second round corrosion test (*7 Appendix A. Test Failure*), several modifications were made to the test system to prevent further failure in the third round of corrosion testing. Instead of the safe but cumbersome hot welding method, a new technique was developed that allowed the crucible to be sealed under vacuum. Prior to assembly, a small access tube was welded to the top of each crucible to facilitate evacuation of the residual argon atmosphere within the crucible. A vacuum pump would be attached once the top was welded to the crucible assembly (Figure 16a). Following suction for two minutes, the vacuum nozzle was crimped to maintain the vacuum and a small section above the crimp was welded shut. The crimp could then be released while maintaining a vacuum pressure inside the crucible (Figure 16b). This vacuum sealing method was thoroughly tested with empty vessels prior to implementing on the corrosion crucibles. All round three corrosion crucibles were tested successfully using the vacuum weld technique.

3.4 Test Matrix

Table 3. Static corrosion test matrix for all three tests. Every test was performed in a 316L crucible held at 850°C for 1000 to 2000 hours.

Crucible	1	2	3	4	5	6	7	8	9	Test Notes
Coupon 1	Haste-N	316L	Haste-N	316L	316L	316L	Haste-N	316L	Haste-N	**Test 1**
Coupon 2	Haste-N	316L	Graphite	Graphite	Graphite	Graphite	Graphite	316L	Haste-N	Inconel furnace
Coupon 3	Haste-N	316L	Haste-N	316L	Haste-N	316L	Haste-N	316L	Haste-N	Cold weld
Redox	None	None	None	None	None	Zr	Zr	Zr	Zr	
Coupon 1	316L	316L	316L	Haste-N	316L	Haste-N	316L	316L	Haste-N	**Test 2**
Coupon 2	316L	Graphite	316L	Haste-N	Graphite	Graphite	316L	Graphite	Haste-N	Low-cost box furnace
Coupon 3	316L	316L	316L	Haste-N	316L	Haste-N	316L	316L	Haste-N	Cold weld
Redox	None	None	Na	Na	Na	Na	None	None	None	Test failed
Coupon 1	316L	316L	316L	Haste-N	316L	Haste-N	316L	316L	Haste-N	**Test 3**
Coupon 2	316L	Graphite	316L	Haste-N	Graphite	Graphite	316L	Graphite	Haste-N	Inconel furnace
Coupon 3	316L	316L	316L	Haste-N	316L	Haste-N	316L	316L	Haste-N	Vacuum weld
Redox	None	None	Na	Na	Na	Na	None	None	None	
Notes	**Control**	**Control**					**2000 hr**	**2000 hr**	**2000 hr**	

As shown in Table 3, three tests were performed in total with two different sample sets. The goal was to test nearly all permutations of alloy, reduction agent, and graphite. In addition, three crucibles were tested for extended periods to examine long term corrosion effects. Crucible one and two in test 3 functioned as control crucibles, where results could be directly compared to the results of crucible two and four in test 1. The comparison of these results seeks to identify any bias introduced by the vacuum sealing method or different batches of FLiNaK.

3.5 Material Preprocessing

Hastelloy-N for the first static corrosion test was procured from ORNL. These samples were milled to the same dimensions as the 316L samples (.5 inch by 1 inch). Hastelloy-N for test two and three was given to UW-Madison by Henry White at Haynes, Inc. (Figure 6) and was cut to a smaller form factor (.25 inch by .75 inch) in order to conserve supplies (Figure 14b). To

eliminate material waste, electrical discharge machining was used. 316L coupons were laser cut from 18 gauge sheet (Figure 14a). All coupons were drilled with diagonally opposing holes for mounting and underwent a polishing process with SiC paper to 1200-grit finish. Following polishing, they were engraved and ultrasonically cleaned in ethanol and deionized water. Lastly, the coupons were dried and weighed on high accuracy microgram scale.

In all corrosion tests, some of the crucibles contained two metallic coupons and one graphite coupon located in the middle slot of the coupon stand (Figure 14b). The purified graphite was procured from POCO, grade AFX-5Q with average particle size of 5 μm and average pore size of 0.8 μm [56]. The graphite was milled to have approximately twice the surface area of a single metallic coupon. Following milling, the graphite was labeled, ultrasonically cleaned in ethanol and deionized water, dried, and weighed. Once all coupons and graphite pieces were tied to the sample rods in the correct order via cleaned 316L wire, they were placed in the glove box to join the salt and other crucible materials.

During the corrosion experiments, the furnace was ramped to 850 ^{o}C at a rate of 200 ^{o}C/hr, then held at 850 ^{o}C for 1000/2000 hours in inert nitrogen atmosphere.

3.6 Material Post Processing

At the conclusion of the 1000/2000 hour testing process, the furnace temperature was lowered to 550 ^{o}C so the crucibles could be removed individually and turned upside down to cool. This caused the salt to solidify while not in contact with the coupons making the sample rod removal easier. The crucible tops were removed with abrasive disc hand saw. Sample rods were pulled from the salt bed and cleaned ultrasonically in 1M $Al(NO_3)_3$ solution to speed the dissolution of the FLiNaK salt, followed by ultrasonic ethanol and DI water bath. The corrosion levels of the samples were evaluated using weight change measurement performed on a Sartorius

microgram scale. Weight change information provides a good qualitative estimate of degree of corrosion in simple systems (that is, comprised of salt and alloy only). When multiple materials are present, weight change can be influenced through electroplating effects or thin film formations, so weight loss becomes a less meaningful indication of material performance and more complex methods must be used to examine the materials. Characterization of the top-view and cross-sectional morphologies of the samples was carried out by scanning electron microscopy (SEM) with energy dispersive spectrometry (EDS), X-ray diffraction (XRD) and electron backscatter diffraction (EBSD).

Solidified FLiNaK salt was examined through inductively coupled plasma optical emission spectroscopy (ICP-OES). The Soil Sciences Laboratory at the University of Wisconsin-Madison performed all ICP-OES processing. ICP-OES allows for parts per million (ppm) accuracy in measuring trace quantities of heavy metals, such as chromium, iron or nickel. Knowing the level of these dissolved species is important in quantifying the degree of corrosion as well as metallic redox agent effectiveness. To acquire accurate ICP-OES measurements, the FLiNaK salt must first be dissolved completely in solution. Fluoride salts are typically very difficult to dissolve to completion in acid, nitrate, or aqueous solutions [17]. Through using a heated, pressurized solution made of a mixture of acids and water, full dissolution could be assured [57]. Neutron Activated Analysis (NAA) is another method used to measure ppm level corrosion species, however the technique is time sensitive and runs into difficulties distinguishing chromium and iron spectra under certain scenarios [58].

4 Results and Discussion

4.1 316L

4.1.1 Weight Change Results

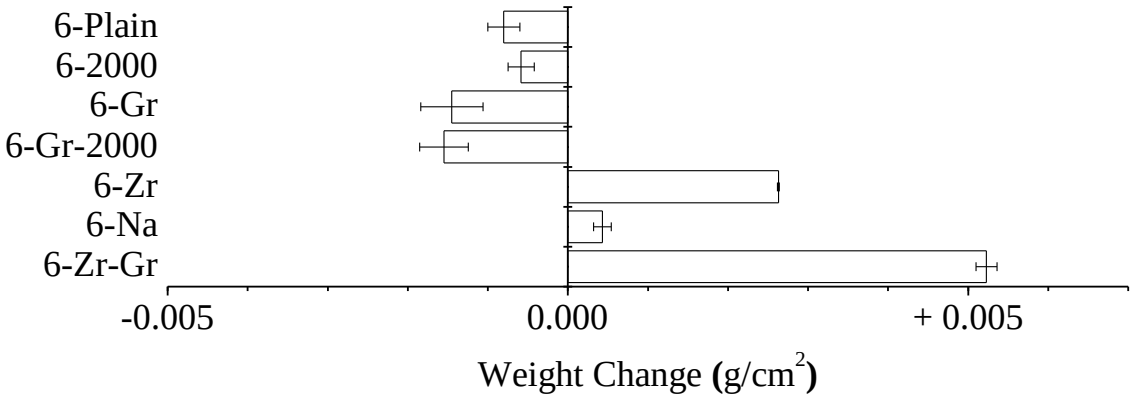

Figure 17. Weight change of all 316L samples exposed to FLiNaK at 850°C for 1000/2000 hours.

Table 4. Weight change details and test parameters of the 316L samples exposed to FLiNaK at 850°C for 1000 or 2000 hours.

Label	Alloy	Additions	Test #	t(h)	T(°C)	Crucible	ΔW (g/cm^2)	σ
6-Na-Gr	316L	Sodium, Graphite	3	1000	850	5	-0.04168	0.00581
6-Zr-Gr	316L	Zirconium, Graphite	1	1000	850	8	0.00523	0.00013
6-Na	316L	Sodium	3	1000	850	3	0.00043	0.00011
6-Zr	316L	Zirconium	1	1000	850	6	0.00263	0.00001
6-Gr-2000	316L	Graphite	3	2000	850	8	-0.00155	0.00030
6-Gr	316L	Graphite	1, 3	1000	850	4, 2	-0.00145	0.00039
6-2000	316L	None	3	2000	850	7	-0.00058	0.00016
6-Plain	316L	None	1, 3	1000	850	2, 1	-0.00080	0.00020

Following removal and cleaning in aluminum nitrate solution, ethanol, and DI water, all 316L samples underwent weight change measurement. A composite table combining weight

changes of all 316L samples exposed to FLiNaK, graphite, and various metallic redox agents can be seen in Table 4.

Generally, all 316L samples in systems containing FLiNaK only or in systems of FLiNaK and graphite lost weight. When metallic redox agents (zirconium and sodium) were present in the system, all 316L samples gained weight. However, there is one exception where surface layer spallation during cleaning caused a large measured weight loss in the test system designated 6-Na-Gr. More details of the process which contributed to the formation of this unstable layer can be seen in section *4.2.5 Severe Phase Instability and Carburization*. Due to the spallation process, true weight change cannot be known.

4.1.2 Surface Chromium Depletion

In simple systems comprised of 316L, FLiNaK, and with or without graphite, the classic FLiNaK attack method on chromium was observed. Figure 18 contains the plan-view and cross-sectional SEM micrographs with the corresponding EDS linescan analysis of 316L samples. EDS elements linescan taken normal to the exposure surface inward show Fe increase and Cr decrease relatively, while Ni and Mo have no change. No alloy phase transformations were observed as evident by γ-austenite detection by surface XRD analysis. These results imply that 316L experienced typical Cr dissolution behavior. Corrosion of 316L is more severe when graphite is present in the system, evident through greater measured weight loss and surface Cr depletion depth. Approximate depth of Cr depletion for 316L and 316L with graphite is 40 μm and 50 μm, respectively. Some voids can also be observed at the grain boundaries near the exposure surface. The formation of these voids is associated with precipitates in 316L at grain boundaries formed during the high temperature, long duration corrosion test, which acted as an annealing process. These phase formations are seen as points of high contract in the 316L cross

section. EDS analysis reveals the composition of these precipitates to be 57Fe-33Cr-4Ni-6Mo (at.%), identified as σ-$(Fe,Ni)_3(Cr,Mo)_2$. The formation of σ-$(Fe,Ni)_3(Cr,Mo)_2$ has been observed in 316L held at 650-900 °C for long periods of time [59]. This elevated Cr content of σ-$(Fe,Ni)_3(Cr,Mo)_2$ over the nominal 18 at.% Cr of the 316L matrix caused σ-$(Fe,Ni)_3(Cr,Mo)_2$ to be preferentially corroded, leading to the void formations. The observation that the size of voids in 316L with graphite present is larger than that in 316L without graphite present also proves the corrosion acceleration effect of 316L by graphite.

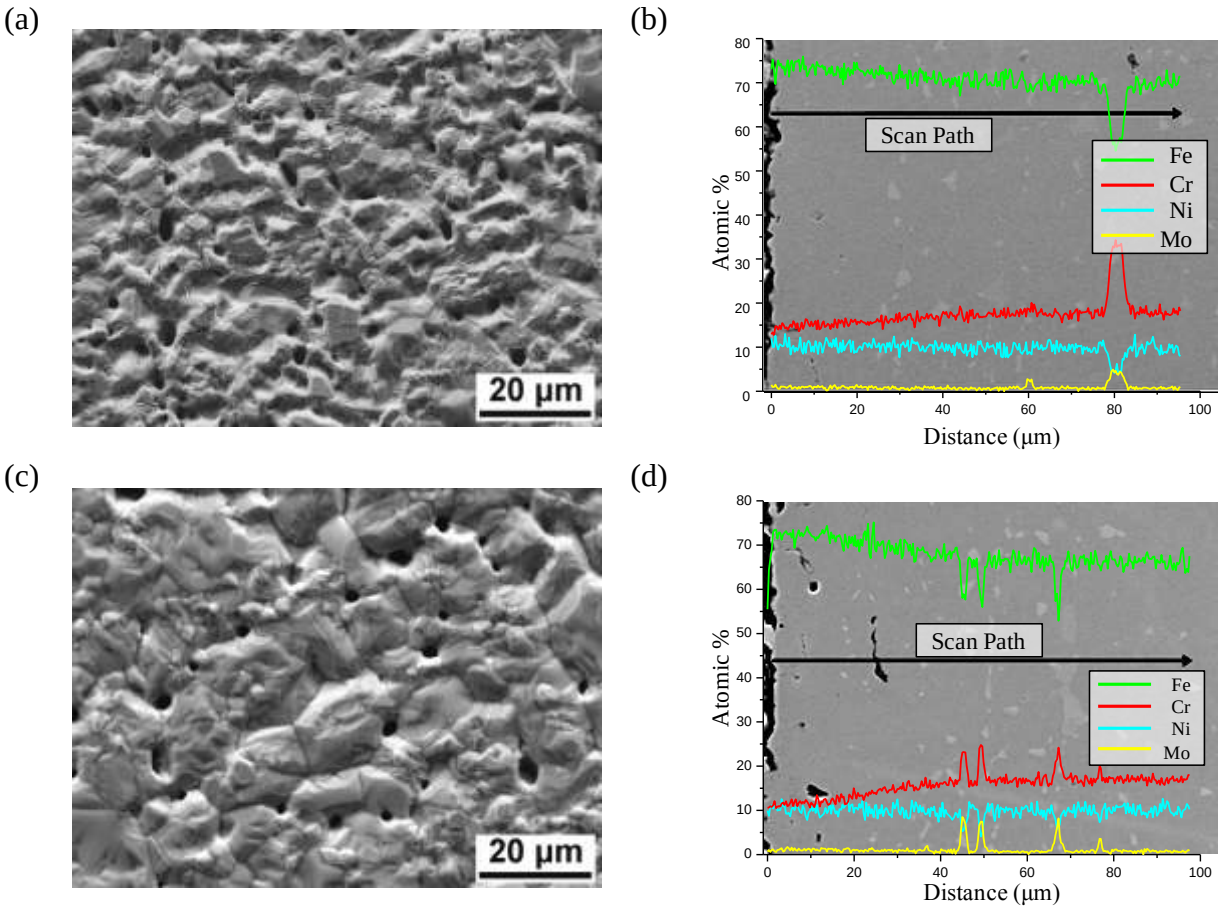

Figure 18. Top-view and cross-sectional SEM micrographs and corresponding EDS linescan analysis of 316L samples tested without graphite (a-b) and with graphite (c-d) in FLiNaK at 850°C for 1000 hours.

4.1.3 Corrosion Test Repeatability

In order to compare results obtained through two different static corrosion tests performed in slightly different test systems, it was necessary to maintain some sample sets which were the same in both static corrosion tests to verify the consistent performance of the two tests. Two crucibles were designated control crucibles. These two crucibles contained either 316L and salt only, or 316L/Salt/graphite. Although the weight loss data from test three is more scattered than in test one, the same general trends are observed in comparison to test one; graphite causes increased weight loss and chromium depletion.

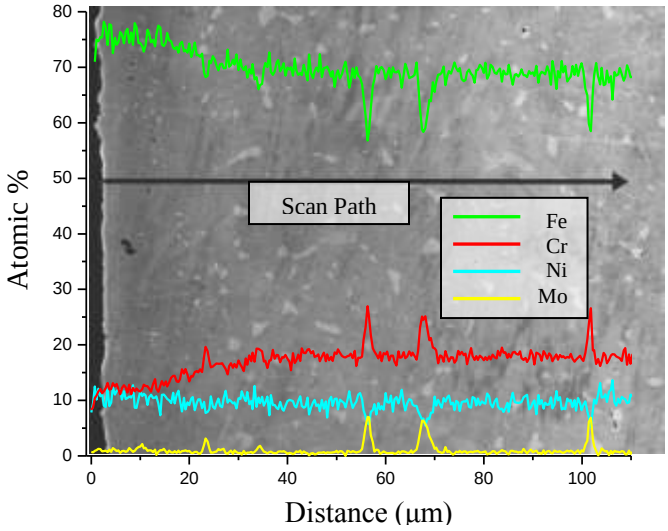

Figure 19. Control crucible round 3 cross-sectional SEM micrograph of 316L exposed to FLiNaK for 1000 hours at 850°C in the presence of graphite.

Figure 19 shows cross sectional characteristics and EDS chromium depletion of a 316L sample in a control crucible from corrosion test 3. The samples from the control crucibles exhibited similar behaviors to the counterpart crucible from test 1, such as enhanced chromium depletion in the presence of graphite, approximately 30-40 micron attack depth and the formation of σ-$(Fe,Ni)_3(Cr,Mo)_2$ phase in the Mo-rich points of high contrast of the SEM micrograph. The

similar results between the first and third round tests demonstrate that the static corrosion test system is repeatable, even though the two tests relied on different salt batches and had different crucible finishing techniques (cold welding vs. vacuum welding).

4.2 316L Material Interactions

4.2.1 Graphite Effect

The presence of graphite causes an increase in weight loss for 316L. In the previous study [16] of materials corrosion in graphite crucibles after FLiNaK exposure at 850^{o}C for 500 hours, it has been shown that all of the iron-based and nickel-based high temperature alloys lost weight. Although 316L was not exposed to FLiNaK in the previous study, it is useful to compare the weight loss measured by L. Olson of Hastelloy-N (~3 mg/cm^2 loss) and Incoloy-800H (~30 mg/cm^2 loss) exposed to FLiNaK in a graphite crucible [16] against the 316L weight loss results of this test (less than 3 mg/cm^2 when in contact with graphite). Conventional wisdom dictates that higher Ni containing alloys should experience less attack; however, it can be seen that the higher Ni containing alloys exposed to FLiNaK by L. Olson lost more weight than the 316L samples exposed in this test. In addition, the exposure time of this test is twice that of the previous test performed by L. Olson. A possible explanation for the disparity is that the area ratio of graphite/sample in the previous study by L. Olson is approximately 170 times larger than the area ratio of graphite/sample in this study. This suggests the area ratio of graphite/sample has a strong effect on the extent of material corrosion, in which the corrosion rate of materials would be accelerated by a larger area ratio of graphite/sample.

For a full characterization of the graphite following corrosion testing see section *4.6 Graphite*.

4.2.2 Zirconium Effect

Figure 17 shows the weight change results of 316L samples in contact with zirconium after corrosion. When Zr was present, all of the samples gained weight after corrosion. The graphite sample in the 6-Zr-Gr system was corroded and broken into small pieces in the molten salt. The weight gain result of 316L samples implies that some materials could deposit on the samples using molten salt as a transporting media.

The top-view and cross-sectional SEM micrographs of 316L samples after corrosion are shown in Figure 20. Both 6-Zr and 6-Zr-Gr samples possess a multiphase coating layer. The thickness of the coating on 6-Zr sample is twice that of the 6-Zr-Gr sample, which were around 12 μm and 6 μm, respectively. From the top-view SEM micrographs, it can be observed that the surface of the coating on 6-Zr sample has a dense structure, while the surface of the coating on 6-Zr-Gr sample possesses a porous structure. Also, some crystals that embedded in the coating only can be found on the 6-Zr sample. Figure 23 is the XRD results of the coating surfaces on 6-Zr and 6-Zr-Gr samples. It shows that Zr_3NiO and $NiZr_2$ were identified on the both samples, while ZrO_2 only existed at 6-Zr sample.

(a) (b)

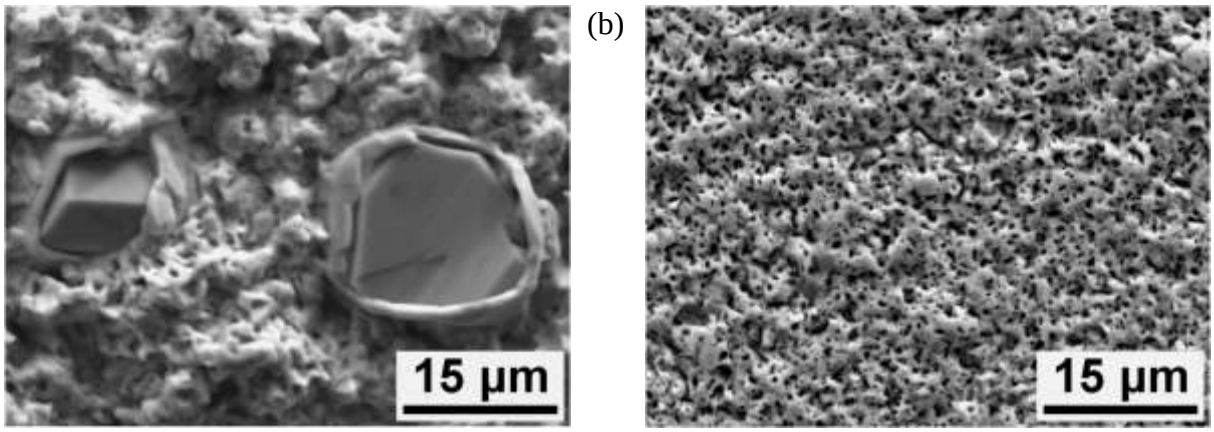

Figure 20. SEM top-view micrographs of (a) 6-Zr and (b) 6-Zr-Gr samples exposed to molten FLiNaK salt at 850°C for 1000 hours.

(a) (b)

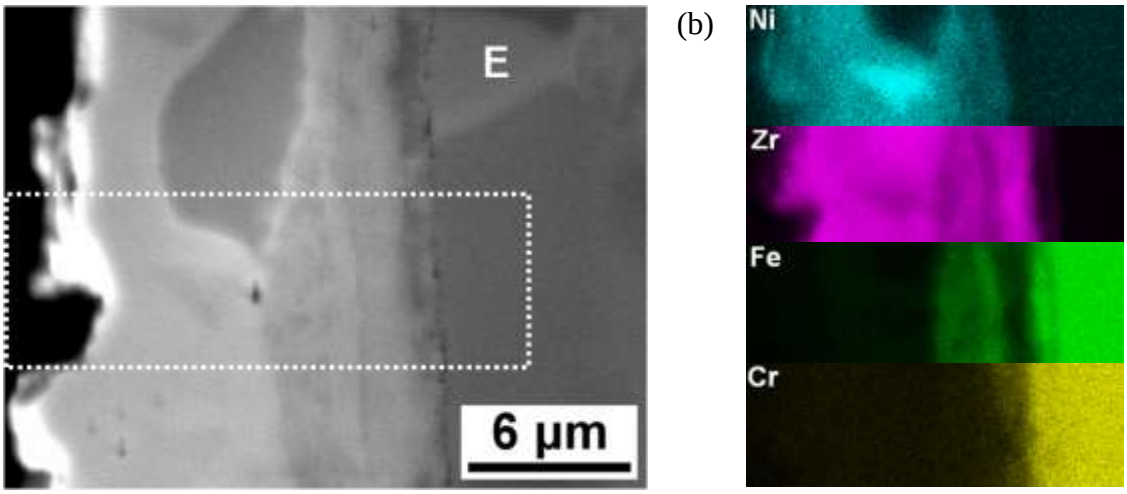

Figure 21. SEM cross-sectional micrographs and EDS distribution of 6-Zr sample system exposed to molten FLiNaK salt at 850°C for 1000 hours.

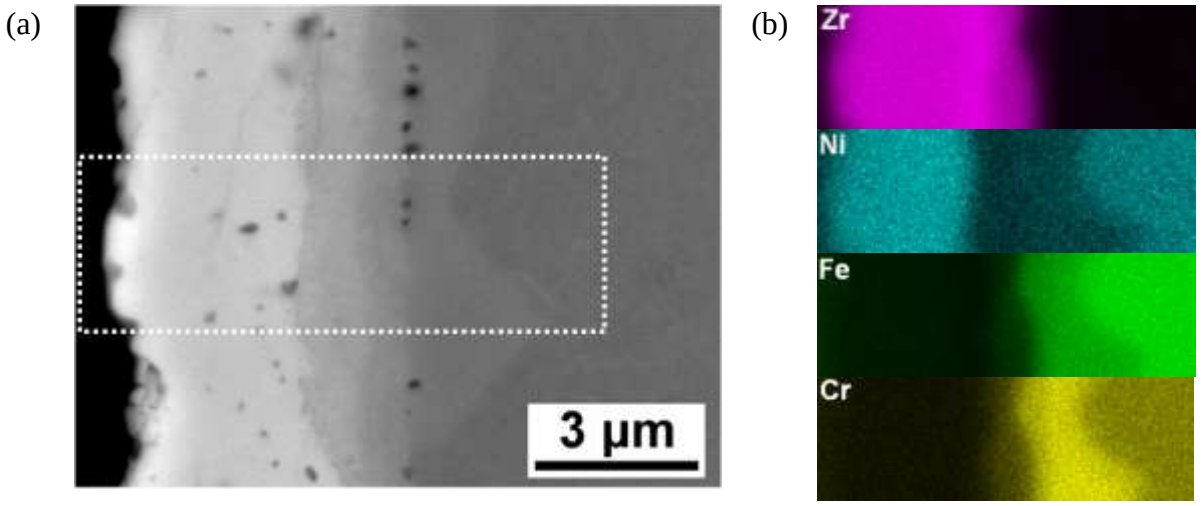

Figure 22. SEM-cross sectional micrographs and EDS distribution of 6-Zr-Gr sample system exposed to molten FLiNaK salt at 850°C for 1000 hours.

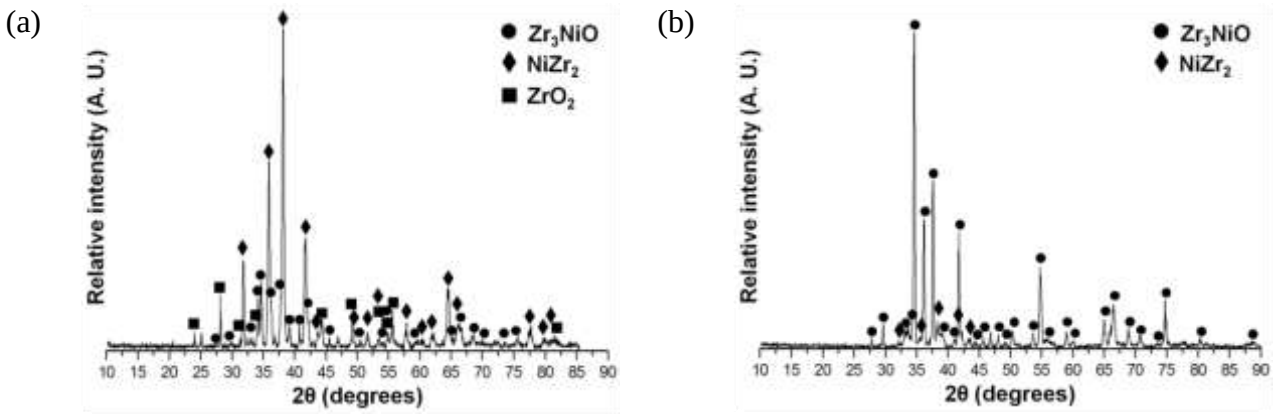

Figure 23. XRD analysis of coating surfaces on (a) 6-Zr and (b) 6-Zr-Gr samples exposed to molten FLiNaK salt at 850 ºC for 1000 hours.

To understand the elemental distribution in the coating, EDS X-ray mapping was performed on a selected rectangular area on the cross-sectional SEM micrograph, as shown in Figure 21 and Figure 22. The coatings on 6-Zr and 6-Zr-Gr possess similar elemental distribution characteristics, that is, comprised primarily of Zr and Ni. The major constituents of 316L, Fe and Cr, however, can only be found at the inner part of the coating. On the other hand, the X-ray mapping results also revealed the locations of the phases with different chemical composition in

the coating. To understand the phase constitution of the coating, the phases exposed by the X-ray mapping are further identified by comparing their EDS measured compositions with the related phase diagrams. The coatings on 6-Zr and 6-Zr-Gr samples are mainly comprised of outer Ni-Zr binary intermetallic phases and inner Fe-Zr binary intermetallic phases, in which Ni, Fe and Cr could substitute for each other within a certain solubility of each phase. Moreover, the embedded crystals found in the coating on 6-Zr sample are identified as ZrO_2 seen in Figure 20a and identified in Figure 23a. From coating surface to substrate, coating on 6-Zr sample is composed of $(Ni,Fe)Zr_2$, ZrO_2, (Ni,Fe)Zr, $(Fe,Ni)_2Zr$, $(Fe,Cr)Zr_2$ and σ-$(Fe,Ni)_3(Cr,Mo)_2$ while coating on 6-Zr-Gr sample is composed of $(Ni,Fe)Zr_2$, $(Fe,Cr)Zr_2$ and σ-$(Fe,Ni)_3(Cr,Mo)_2$ [60-63].

4.2.3 Performance Speculation

The tendency for alloying constituents in 316L to be attacked in molten fluoride salts increases in the following order: Ni, Fe, and Cr [16]. Zr addition in molten FLiNaK salt caused the formation of a coating, containing mainly Zr and Ni, on the 316L samples. Thus, the coatings behave as a barrier layer by restraining the outward diffusion of Fe and Cr through the preferential movement of Ni. This effectively protects the substrate from further corrosion since from a thermodynamic sense Ni is relatively noble as well as the closest alloying constituent to the surface. However, the coatings on the 316L are composed of major Ni-Zr intermetallic phase which is more brittle than the metallic substrate. Also, the thermal expansion coefficient mismatch between coating and substrate can result in cracking in the coating when the samples undergo thermal shock or thermal cycling [64].

4.2.4 Sodium Effect

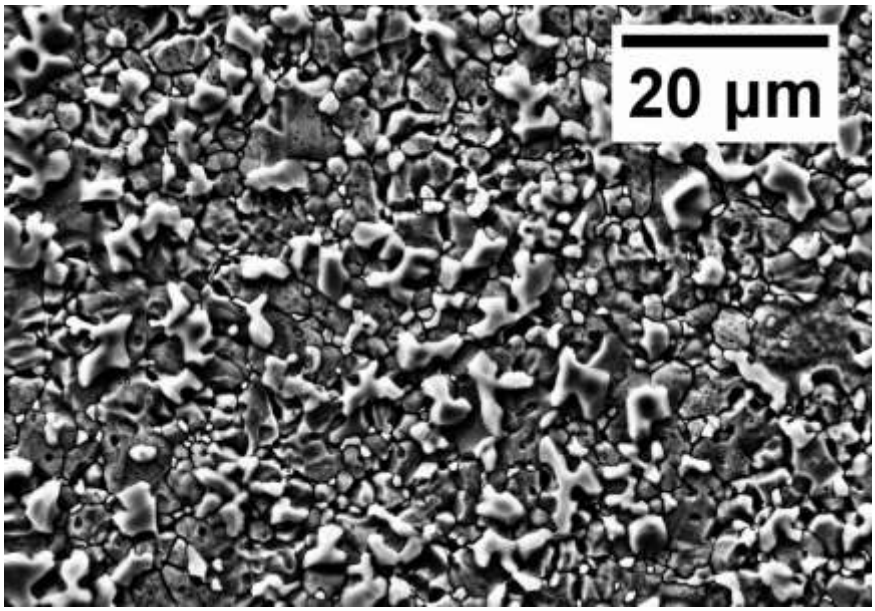

Figure 24. Plan view SEM micrograph of 316L exposed to FLiNaK with sodium for 1000 hours at 850°C.

(a)

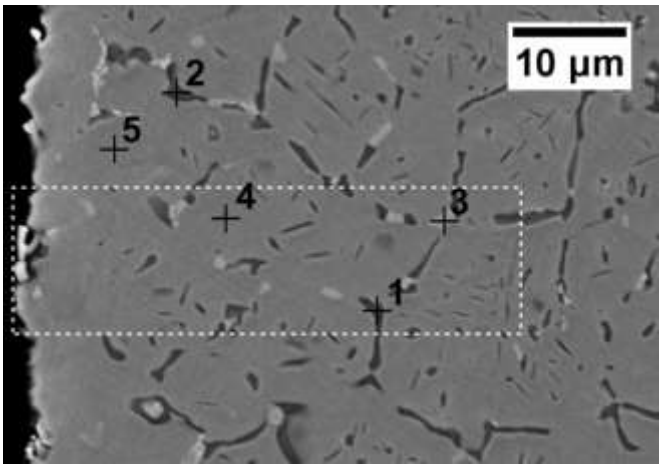

(b)

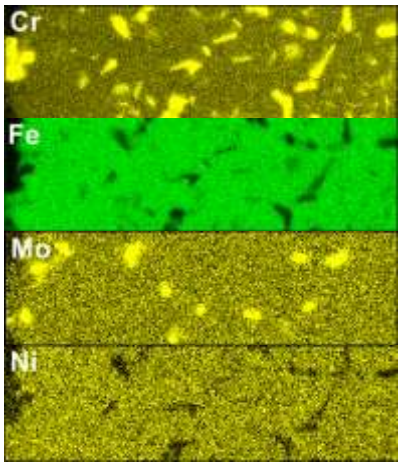

Figure 25. Cross-sectional SEM micrograph and EDS element distribution of 316L exposed to FLiNaK salt for 1000 hours at 850°C with metallic sodium added as a reduction agent.

Table 5. EDS composition of several points taken from 316L exposed to FLiNaK with metallic sodium for 1000 hours at 850°C.

Number	EDS Chemical Composition (at. %)						
	Cr	Mn	Fe	Ni	Mo	Si	V
1	69.1	1.0	24.4	3.0	1.0	-	1.5
2	84.8	1.0	10.1	1.2	1.0	-	1.9
3	19.1	2.0	58.9	4.7	10.0	2.4	-
4	13.4	1.9	72.4	9.9	1.0	1.4	-
5	12.7	1.7	73.6	9.5	.9	1.5	-

Similar to crucibles exposed to metallic zirconium, 316L was exposed to metallic sodium in two scenarios: without graphite and with graphite, designated 6-Na and 6-Na-Gr respectively. Weight loss characteristics for both can be seen in Table 4. Above, shown in Figure 24 and Figure 25 are SEM micrographs with corresponding EDS elemental analysis for sample 6-Na. There are several interesting phenomena happening in this scenario. The plan view and cross sectional micrographs show three different prominent phase formations: bright/high contrast nodes, dark intergranular formations. and the stainless steel matrix.

The high contrast nodes, identified in point 3 of Table 5, are suspected to be σ-$(Fe,Ni)_3(Cr,Mo)_2$ phase formations. This sigma phase formation has been observed in 316L held at 650-900 °C for long periods of time [59] and is a common occurrence among these high temperature corrosion tests. As can be seen in Figure 26, the sigma phase formation permeates uniformly through the thickness of the sample, suggesting it is a heat effect and not dependant on the chemical environment. These formations can also be observed in test 1 316L cross sections seen in Figure 18 and Figure 19 (samples designated 6-Plain and 6-Gr). However, it is important to note that due to near surface chromium depletion, the SEM cross sections of Figure 18 and Figure 19 lack sigma phase formations up to 15-25μm from the surface. The sigma phase formations shown in Figure 25 exist up to the surface as well as on the surface. Combined with a

nearly negligible weight change shown in Figure 17, this result suggests that the 6-Na system did not show preferential attack towards chromium due to the addition of sodium as a redox agent.

The salt appearance of crucible set 6-Na seen in Figure 30a is noteworthy. Of all FLiNaK test systems, this crucible emerged the cleanest looking, indicative of pure salt with few corrosion products dissolved.

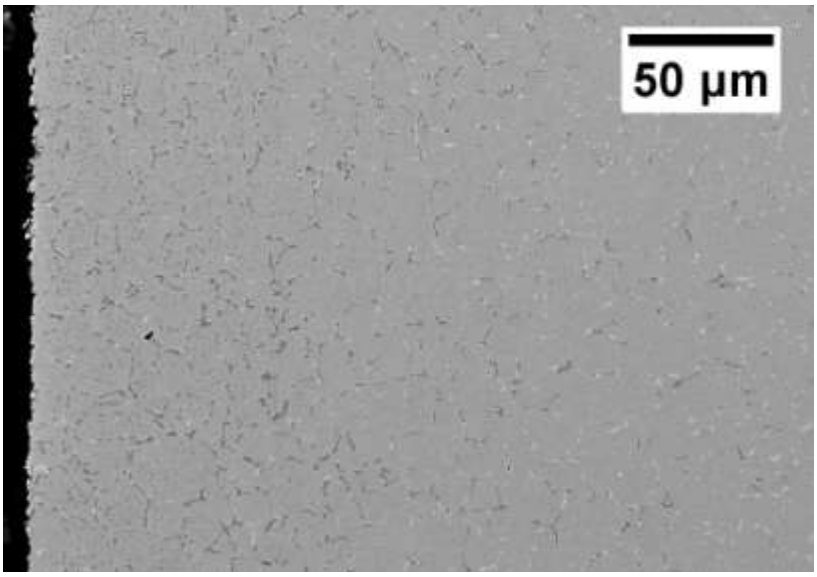

Figure 26. Cross-sectional SEM micrograph of 316L sample 6-Na. The image illustrates the near surface concentration of the dark intergranular phase formation and the uniform dispersion of σ-$(Fe,Ni)_3(Cr,Mo)_2$.

On the other hand, the dark phases are a surprising effect and were not observed in any previous tests. Unlike σ-$(Fe,Ni)_3(Cr,Mo)_2$, these formations are composed primarily of Cr and Fe. Seen in Table 5 points 4 and 5, these phase formations effectively reduce the 316L matrix chromium content from the normal 17 at% to around 13 at% by segregating the chromium to these dark phase formations. The segregation of chromium has also made the 316L alloy slightly magnetic, suggesting that the coupon structure has deviated from the typically nonmagnetic austenitic γ(Fe, Ni) phase. Unlike the sigma phase formation, the dark phase formation is more prominent near the exposure surface, shown in Figure 26. This result suggests that the addition of sodium somehow initiated the near surface dark phase transformation.

4.2.5 Severe Phase Instability and Carburization

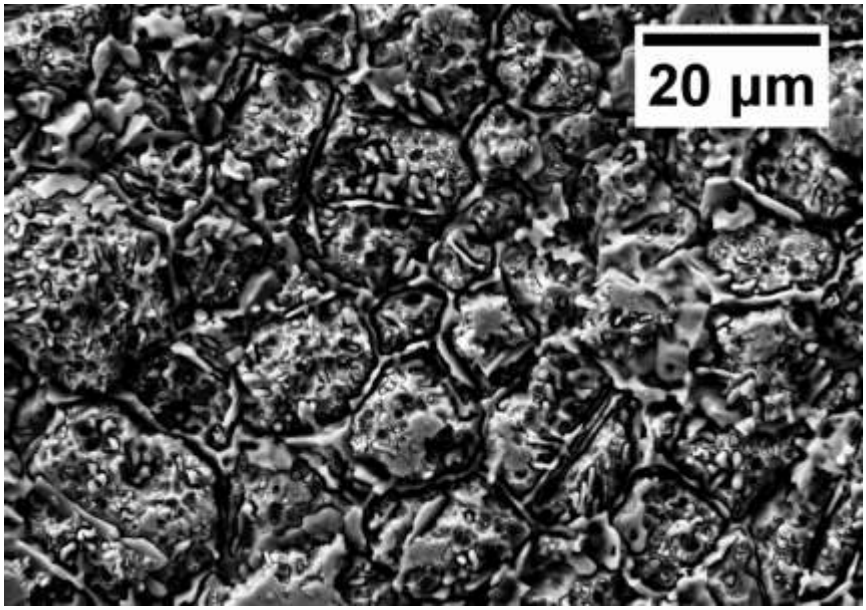

Figure 27. Plan view SEM micrograph of 316L exposed to FLiNaK with sodium and graphite for 1000 hours at 850°C. Sample designation 6-Na-Gr.

(a)  (b) 

Figure 28. 316L sample exposed to FLiNaK with sodium and graphite for 1000 hours at 850°C at the conclusion of the test (a) and following cleaning (b).

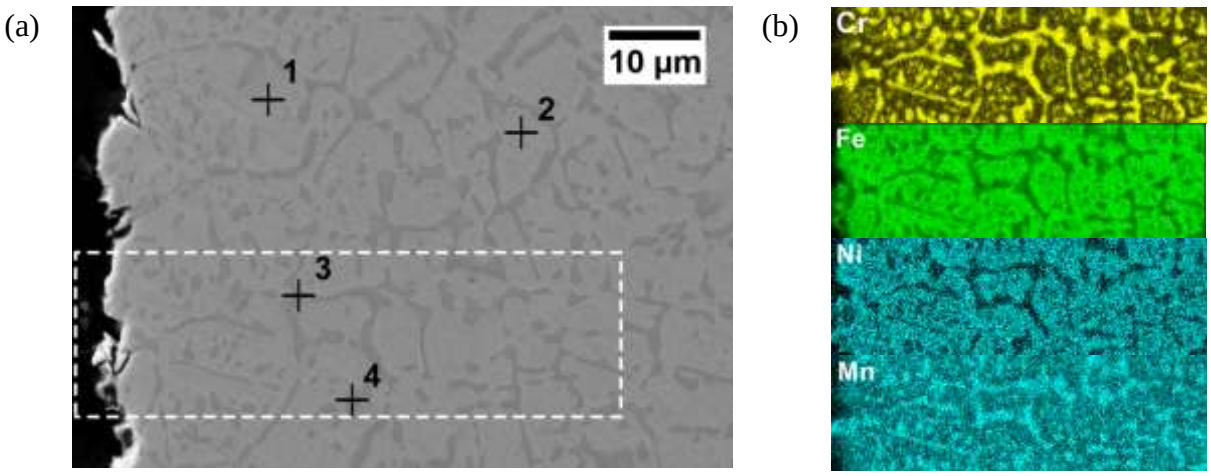

Figure 29. Cross-sectional SEM micrograph and EDS element distribution of 316L exposed to FLiNaK salt and graphite for 1000 hours at 850°C with metallic sodium added as a reduction agent.

Table 6. EDS composition of several points taken from 316L exposed to FLiNaK with graphite and metallic sodium for 1000 hours at 850°C.

Number	EDS Chemical Composition (at. %)						
	Cr	Mn	Fe	Ni	Mo	Si	C
1	12.5	1.8	66.7	9.5	1.3	1.3	6.9
2	14.5	-	65.9	9.3	1.1	.9	7.7
3	35.7	1.8	44.6	2.7	1.2	-	14
4	35.8	2.1	43.6	2.4	1.4	-	14.7

Significant damage to the 316L coupon was observed in crucibles containing FLiNaK, sodium, and graphite. Following removal from the furnace, the test material appeared to be intact as shown in Figure 28a. The engraved serial number was easily visible on each coupon and no obvious damage could be seen. However, over the course of the three step cleaning process, significant surface spallation occurred which resulted in the loss of the entire silver layer from each coupon (Figure 28b). As a result, the recorded weight loss is extremely high and not necessarily meaningful. The plan view SEM micrograph can be seen in Figure 27. Similar to

Figure 24, there are many different phase formations, notably chromium rich intergranular formations.

(a)  (b) 

Figure 30. FLiNaK cross sections for sample sets (a) 6-Na and (b) 6-Na-Gr. Black graphite particles seen in (b) are indications of graphite damage by sodium.

The graphite in this crucible was completely disintegrated into the salt and was not recovered, shown in Figure 30b. It is thought that an intercalation process between the graphite and sodium occurred, leading to the destruction of the graphite sample. Interestingly, the 316L samples from the 6-Na-Gr test group all became strongly magnetic following the conclusion of the test. This is further proof of a phase instability phenomena induced by a combination of sodium and graphite. It is hypothesized that the growth in available graphite surface area may have caused a localized increase in carbon content of the stainless steel, causing the stainless steel to undergo a phase transformation away from the nonmagnetic austenite crystalline structure. Increasing the surface area of the graphite could cause further attack on chromium as demonstrated in Figure 18. The silver coupon surface shown in Figure 28a is likely the region most affected by carburization and therefore the most unstable.

The vastly different 316L microstructure of the 6-Na batch from 6-Zr, 6-Gr and 6-Plain warrants further investigation. Two different 316L batches were used over the course of the two

tests, so it may be possible that the effect may have been caused by a slight difference in sheet production, material handling, or sample preparation.

4.3 316L Transient Effect

To observe time dependent effects of 316L corrosion in molten FLiNaK salt at 850°C, two crucibles were tested for an extended duration of 2000 hours (approximately 12 weeks). One crucible contained only 316L, the other contained 316L and a standard graphite coupon. By observing weight gain, chromium depletion levels, and chrome carbide deposition thickness, conclusions can be drawn as to the rate nature of the corrosion process: linear vs. exponential vs. logarithmic. Transient weigh change characteristics can be seen in Figure 31. It can be seen from this figure that an extended 2000 hour exposure time had no significant effect on weight change. There were no surprise behaviors when graphite was introduced in the system; graphite caused a corresponding increase in weight loss through the chrome carbide effect just as in sample sets heated for 1000 hours. There were no significant changes in physical characteristics of the 2000 hour samples.

Negligible increase in weight loss for an extended duration test is an important and positive result. The result suggests corrosion in this test system occurs though a large initial corrosion process, which quickly decreases to negligible levels. Small quantities of impurities present in the system in the form of water or unstable metallic fluorides are likely the source of initial chromium attack. However, due to a lack of dependable impurity measurements of the salt, it is unknown if this corrosion drop off is due to these impurities quickly being ‘used up’ by reduction to more stable fluoride compounds, or if corrosion product solubility limits are reached within the salt.

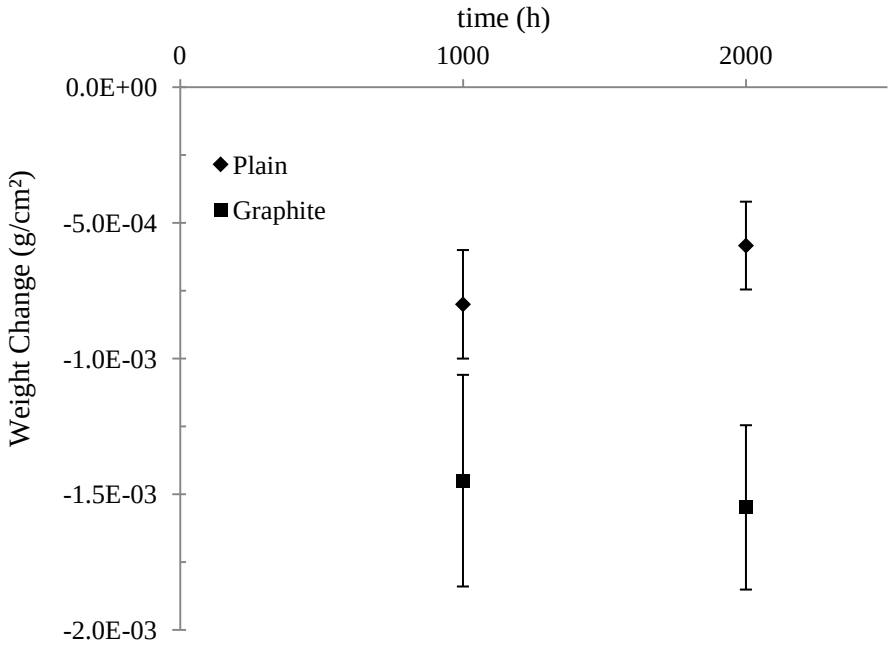

Figure 31. Weight comparison between static corrosion tests containing 316L stainless steel and/or graphite held at 850°C in FLiNaK molten salt for 1000 and 2000 hours.

In test systems containing simple sample sets, that is, no redox agent, weight change is an accurate predictor for the degree of corrosion. It can be expected that chromium depletion levels for the 2000 hour sample sets correspond well to the matching 1000 hour sample set.

(a) (b)

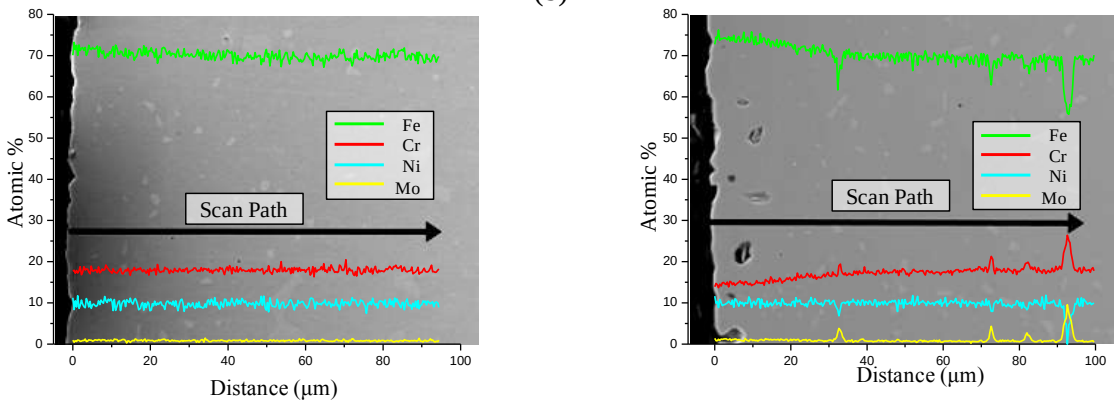

Figure 32. Cross-sectional SEM micrographs and corresponding EDS linescan analysis of 316L samples tested without graphite (a) and with graphite (b) in FLiNaK at 850°C for 2000 hours.

SEM cross-sectional micrographs and corresponding EDS elemental line scan compositions for 2000 hour exposed sample sets can be seen in Figure 32. As in samples exposed for 1000 hours (Figure 18), crucibles containing graphite showed a marked decrease in chromium concentration at the exposure surface. However, shown in Figure 32a, there is no significant change in chromium surface concentrations for the 2000 hour exposure sample containing no graphite (sample designated 6-2000) even though there was measured weight loss. What likely occurred was diffusion of chromium towards the surface from the substrate over the course of the 2000 hours, in effect "filling in" chromium which had been depleted by initial attack by FLiNaK. This filled in chromium was left alone either because there were no more impurities to spur corrosion, or chrome solubility limits were reached in the FLiNaK.

Samples containing graphite showed similar weight loss levels compared to corresponding 1000 hour crucible, but surface chromium concentrations are higher in samples exposed for 2000 hours. This can be explained by the effect described previous, whereby chromium migrates into metallic regions containing less chromium.

Also, high contrast σ-$(Fe,Ni)_3(Cr,Mo)_2$ phase formations can be seen. This phase formation has been established as a heat effect, whereby heating at 850°C for a long duration of time acts as a heat treatment process. The sigma phase formation for the 2000 hour samples is approximately the same size as samples exposed for 1000 hours. Voids are also visible in the 2000 hour sample containing graphite. Like the 1000 hour counterpart, these voids are likely due to the selective attack of chromium rich pockets of sigma phase precipitate.

4.4 Hastelloy-N

4.4.1 Weight Change Results

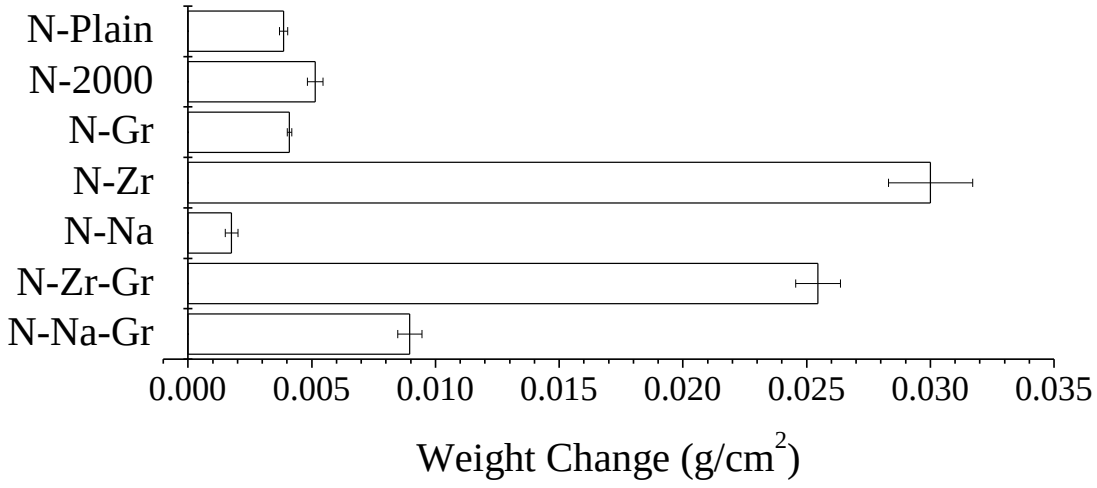

Figure 33. Weight change of all Hastelloy-N samples exposed to FLiNaK at 850°C for 1000/2000 hours.

Table 7. Weight change details and test parameters of the Hastelloy-N samples exposed to FLiNaK at 850°C for 1000/2000 hours.

Label	Alloy	Additions	Test #	t(h)	T(°C)	Crucible	ΔW (g/cm^2)	σ
N-Na-Gr	Hastelloy N	Sodium, Graphite	3	1000	850	6	0.00896	0.00049
N-Zr-Gr	Hastelloy N	Zirconium, Graphite	1	1000	850	9	0.02546	0.00090
N-Na	Hastelloy N	Sodium	3	1000	850	4	0.00176	0.00026
N-Zr	Hastelloy N	Zirconium	1	1000	850	7	0.03001	0.00170
N-Gr	Hastelloy N	Graphite	1	1000	850	3	0.00410	0.00009
N-2000	Hastelloy N	-	3	2000	850	9	0.00514	0.00032
N-Plain	Hastelloy N	-	1	1000	850	1	0.00386	0.00017

Contrary to the corrosion behavior of the 316L coupons, all Hastelloy-N samples gained weight while exposed to FLiNaK at 850 ^{o}C for 1000 hours. This result implies that material deposited on Hastelloy-N using molten salt as a transport media. It bears repeating that all Hastelloy-N samples were contained in a 316L crucible, so there are additional galvanic effects

caused by the differing electromotive potentials of the Fe-Cr-Ni 316L and the Ni-Mo-Cr Hastelloy-N. However, the impact of graphite and redox agents was not overshadowed by the galvanic cell effect.

4.4.2 Crucible Effect on Hastelloy-N Corrosion

(a) (b)

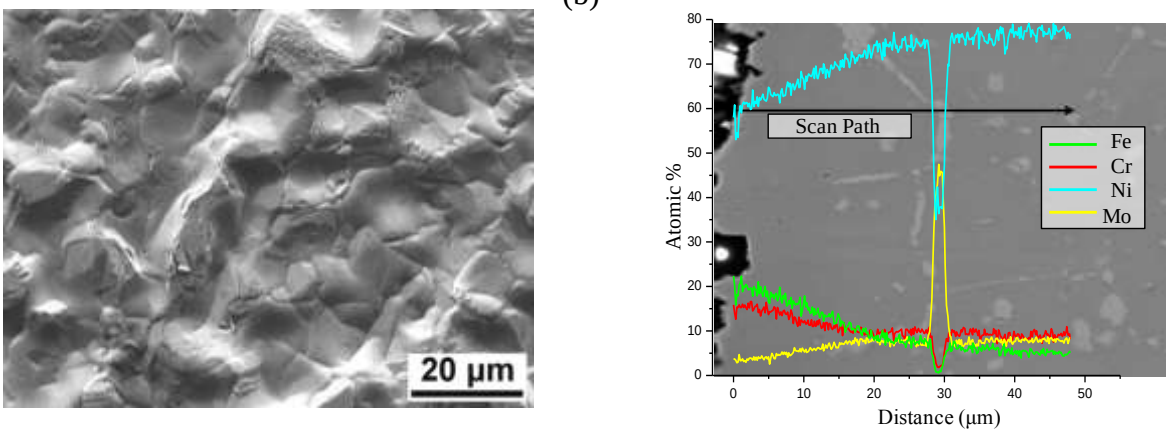

Figure 34. Top-view and cross-sectional SEM micrographs and corresponding EDS linescan analysis of Hastelloy-N samples tested without graphite in FLiNaK at 850°C for 1000 hours.

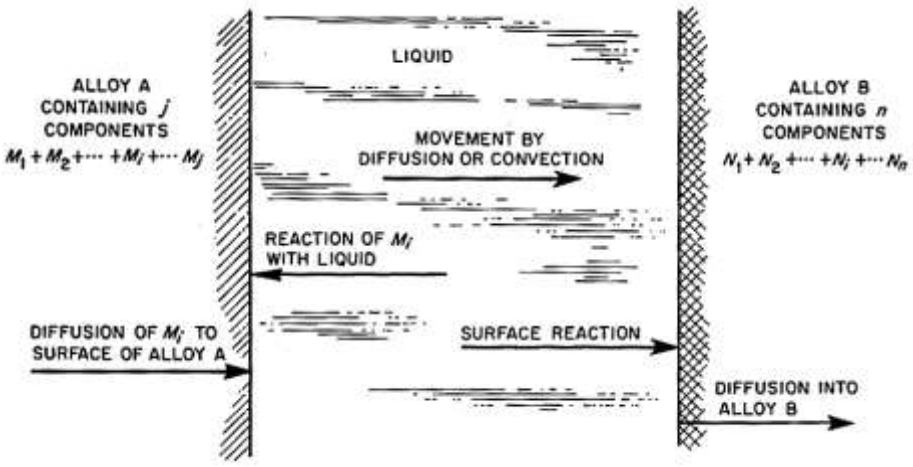

Figure 35. Schematic explanation of species movement between differing alloys within high temperature molten salt [46]**.**

Table 8. EMP series for transition metal ions in molten FLiNaK at 750˚C in reference to the standard potential of a Ni2+/Ni couple that was set to zero [28]**.**

Half Cell Reaction	Standard potential (volts vs. standard Ni^{2+}/Ni electrode)
$Ni^{2+} + 2e^- = Ni$	0
$Fe^{3+} + 3e^- = Fe$	-0.21
$Fe^{2+} + 2e^- = Fe$	-0.512
$Cr^{2+} + 2e^- = Cr$	-0.69
$Cr^{3+} + 3e^- = Cr$	-1.13
$Zr^{4+} + 4e^- = Zr$	-1.25

Top-view SEM micrographs of N-Plain (Hastelloy-N without graphite present) display the morphology of polyhedral-shaped grains on the surface (Figure 34a), which indicated Hastelloy-N underwent diffusion process. Figure 34b shows the cross-sectional SEM micrographs and corresponding EDS linescan analysis of Hastelloy-N samples which were not in contact with graphite, designated N-Plain. From the inner substrate to the sample surface, Fe and Cr linescan profiles increased while Ni and Mo linescan profiles decreased, suggesting Ni/Mo dissolution. However, this conclusion is contrary to the nature of materials corrosion in FLiNaK, in which Ni and Mo are more passive than Fe and Cr. Although the XRD analysis shows the crystal structure of the sample surface is γ-austenite, which is the same as Hastelloy-N, the weight gain of Hastelloy-N and the formation of the Fe and Cr rich outer layer give strong evidence of a Fe/Cr deposit process instead of Ni/Mo dissolution. Similar result has been described by Kondo et. al. [22, 23]. Due to the large Ni content of Hastelloy-N, it is believed the coupons acted as a cathode whereby corrosion products (Fe and Cr) dissolved from the 316L crucible and plated to the surface of Hastelloy-N. This deposit process is explained through the position of Ni on electromotive potential (EMP) series in molten FLiNaK salt as shown in Table 8. Ni is more electropositive than Fe and Cr thus acts as a cathode. The Fe and Cr deposit on the Hastelloy-N surface spurred the inward diffusion of Fe and Cr and outward diffusion of Ni and

Mo. Figure 35 shows in very simple terms the process of species migration within the molten FLiNaK salt. In this scenario, alloy A, the material donating the diffusion species, is 316L and alloy B, the recipient of the dissolved Fe/Cr species, is Hastelloy-N.

4.5 Hastelloy-N Materials Interaction

4.5.1 Graphite Effect

(a) (b)

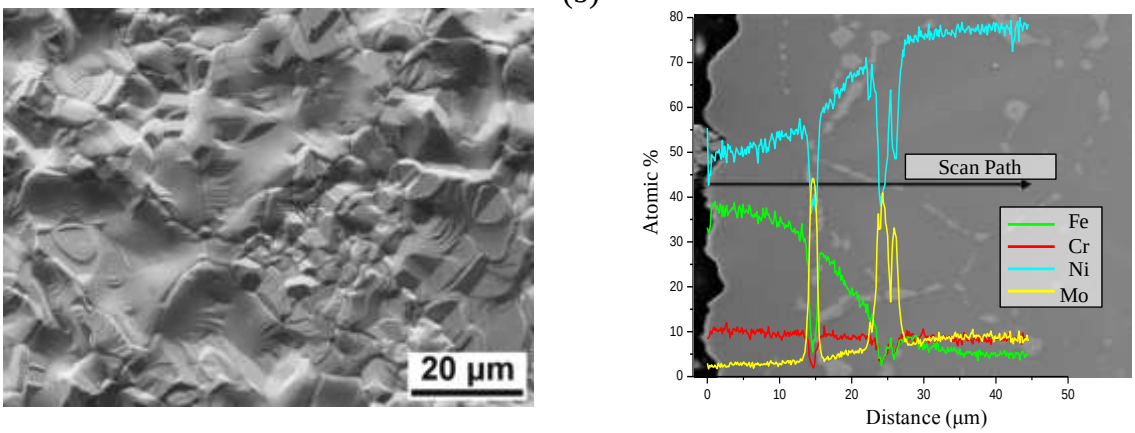

Figure 36. Top-view and cross-sectional SEM micrographs and corresponding EDS linescan analysis of Hastelloy-N samples tested with graphite in FLiNaK at 850°C for 1000 hours.

The top-view and cross-sectional SEM micrographs and corresponding EDS linescan analysis (Figure 36) reveal Hastelloy-N with presence of graphite underwent the same Fe and Cr deposit process as Hastelloy-N without presence of graphite (Figure 34). However, the presence of graphite influenced the composition of the deposited layer to contain more Fe and less Cr, resulting in larger substrate Ni diffusion. The reason for this is due to the deposit formation on the graphite surface caused by the nonelectric transfer effect between graphite and 316L crucible, The graphite deposit has the same microstructure as observed on the graphite tested with 316L samples, major $(Cr,Fe)_7C_3$ with small amount of $(Mo,Cr,Fe)_2C$ particles. Thus, graphite can be

seen as a Cr sink causing a decrease in the amount of Cr available to plate to the surface of the Hastelloy-N sample, resulting in the proportional increase of Fe in the deposit on Hastelloy-N. Since more Fe deposited on the Hastelloy-N, more Ni from the substrate could diffuse outward. As can be seen in section *4.6.1 Carbide Alloying Effect*, the formation of $(Mo,Cr,Fe)_2C$ demonstrates that graphite causes Mo dissolution of the 316L crucible. The same mechanism for Mo dissolution should also happen to the Hastelloy-N sample because it has a larger Mo content (~16 wt.%). However, the deposit of Fe and Cr covered the Hastelloy-N sample and impeded the exposure of the sample to FLiNaK. The speculation of Mo dissolution from Hastelloy-N warrants further investigation.

4.5.2 Zirconium Effect

Figure 36 displays the top-view and cross-sectional SEM micrographs of Hastelloy-N samples after corrosion. The multiphase coatings can be found on N-Zr and N-Zr-Gr samples. The coatings on N-Zr and N-Zr-Gr have similar cross-sectional microstructures as well as thicknesses (~65 μm). A microstructural difference between coatings on N-Zr and N-Zr-Gr samples is that the coating on N-Zr possesses a larger number and size of embedded crystals than the coating on N-Zr-Gr sample. Also, the top-view SEM micrographs of the coating on N-Zr and N-Zr-Gr samples reveals that the coating surface of N-Zr has a dense structure, while the coating surface of N-Zr-Gr has a porous structure. The coating surfaces on N-Zr and N-Zr-Gr samples have the similar XRD result to the 6-Zr and 6-Zr-Gr samples, in which Zr_3NiO, ZrO_2 and NiZr were identified on N-Zr samples, while Zr_3NiO and $NiZr_2$ were found on N-Zr-Gr sample.

(a) (b)

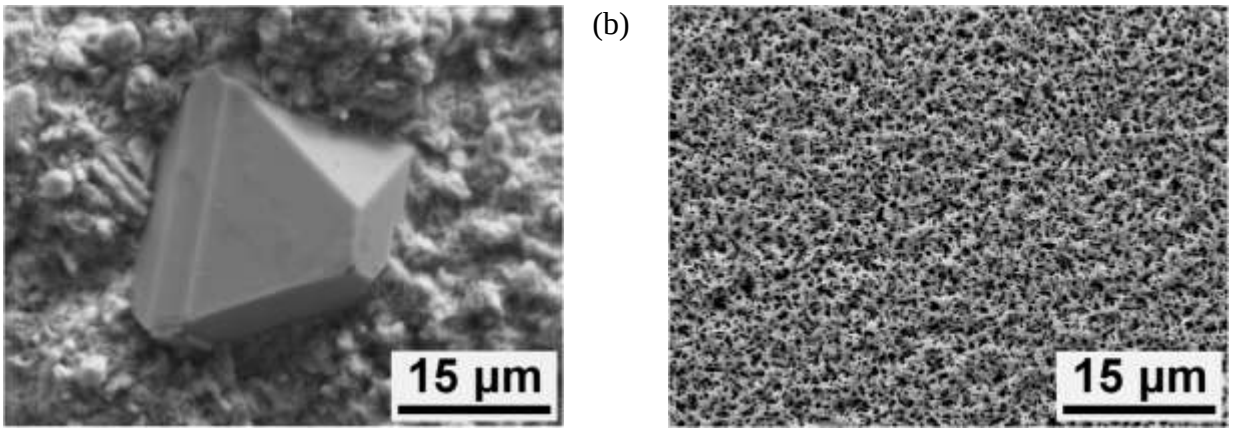

Figure 37. SEM top-view micrographs of (a) N-Zr and (b) N-Zr-Gr samples exposed to molten FLiNaK salt at 850°C for 1000 hours.

(a) (b)

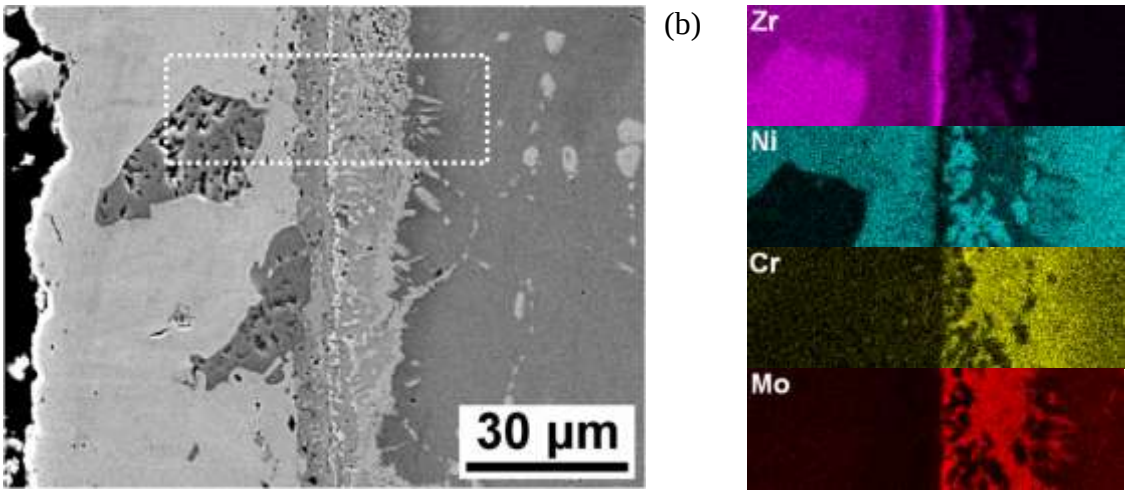

Figure 38. SEM cross-sectional micrographs and EDS distribution of N-Zr sample system exposed to molten FLiNaK salt at 850°C for 1000 hours.

(a) (b)

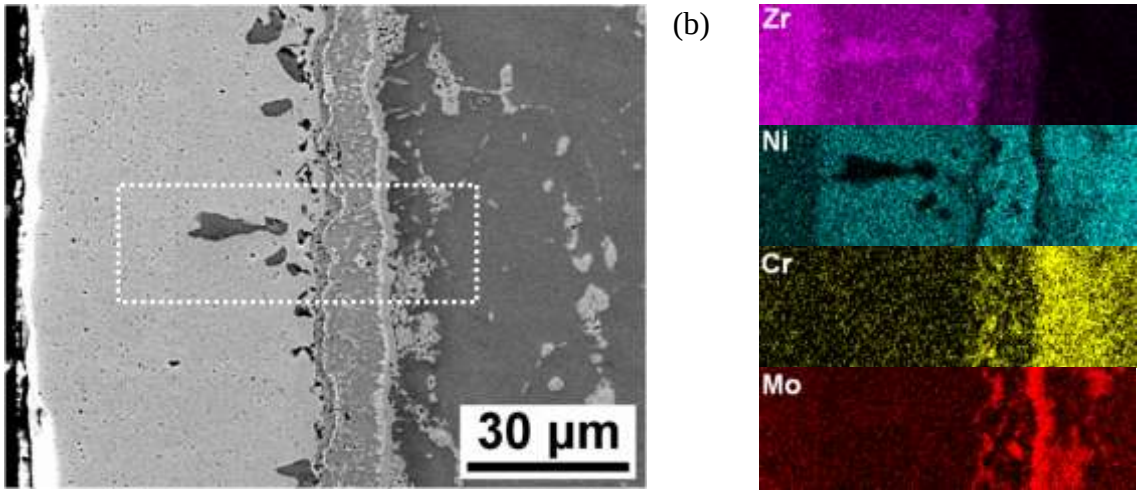

Figure 39. SEM cross-sectional micrographs and EDS distribution of N-Zr-Gr sample system exposed to molten FLiNaK salt at 850°C for 1000 hours.

EDS X-ray mapping results of the selected rectangular area on cross-sectional SEM micrographs of the coatings on N-Zr and N-Zr-Gr are shown in Figure 38 and Figure 39. The coatings on N-Zr and N-Zr-Gr possess the similar characteristics of elemental distributions, and are composed of mainly Zr and Ni. In the inner part of coatings on N-Zr and N-Zr-Gr, the concentrations of Mo and Cr, the second and third major alloying elements in Hastelloy-N, are higher than their nominal concentration in the substrate. On the other hand, Al and Si element distribution maps revealed an Al-rich layer and a Si-rich layer formed above the Mo and Cr-rich phase in the coating on N-Zr, and a Si-rich layer formed above the Mo and Cr-rich phase in the coating on N-Zr-Gr.

The distribution of the Ni-Zr phases from the coating surface to substrate is $NiZr_2$, NiZr, $Ni_{10}Zr_7$ and Ni_7Zr_2, respectively. Among these Ni-Zr phases, the $NiZr_2$ phase only formed in the coating on N-Zr, while $Ni_{10}Zr_7$ is only present in the coating on N-Zr-Gr. The Mo and Cr-rich phase observed in the inner part of the coating is identified as (Mo,Cr) solid solution phase and σ-$Cr_{0.4}Mo_{0.3}Ni_{0.3}$ ternary intermetallic phase. The Al-rich layer in the coating on N-Zr and Si-rich layer in the coatings on N-Zr and N-Zr-Gr are confirmed as Ni_2ZrAl and NiZrSi, respectively.

The embedded crystals formed in the coatings on N-Zr and N-Zr-Gr are recognized as ZrO_2 [62, 63, 65-67].

4.5.3 Substrate Depletion by Zr Coating Formation

The phase constitution results of the coatings have shown that Ni-Zr binary intermetallic phases are the main constituents of the coatings on Hastelloy-N substrates. This implies that Ni is the major outward diffusion element, forming a Ni depleted zone. The depth of the Ni depleted zone can be termed as substrate depletion, which is the distance between coating/substrate interface and remaining good substrate (substrate containing its nominal composition). Generally, the Hastelloy-N sample has relatively larger substrate depletion than the 316L sample. The substrate depletion is proportional to the weight change.

4.5.4 Sodium Effect

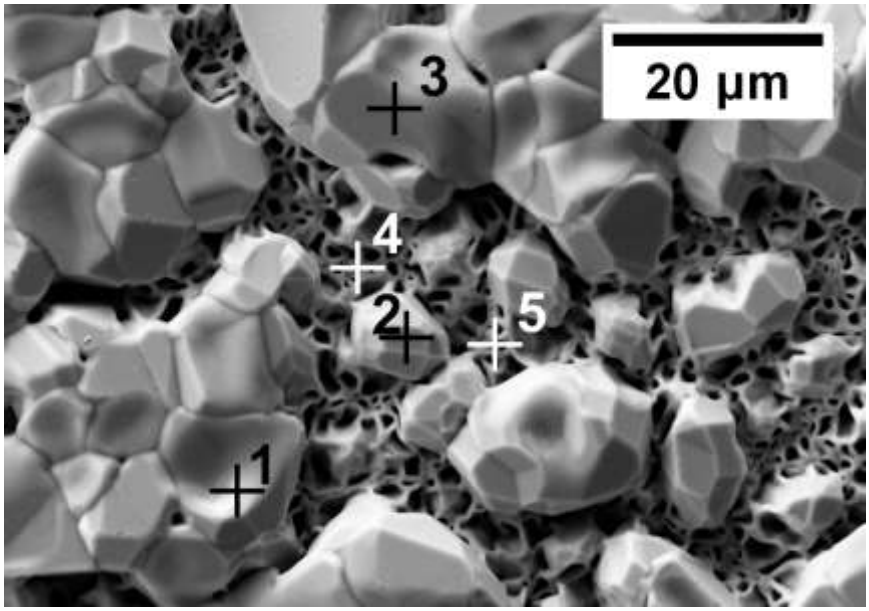

Figure 40. Plan view SEM micrograph of Hastelloy-N exposed to FLiNaK with sodium for 1000 hours at 850°C. Sample designation N-Na.

Table 9. EDS composition of several points taken from Hastelloy-N exposed to FLiNaK with metallic sodium for 1000 hours at 850°C.

Number	EDS Chemical Composition (at. %)						
	Al	Si	P	Cr	Fe	Ni	Mo
1	8.2	20.6	-	1.8	1.9	67.5	-
2	6.6	16.1	-	2.0	2.0	73.2	-
3	6.8	16.9	-	2	1.9	71.7	0.6
4	1	20.2	3.3	6.1	0.7	57	11.3
5	1.3	21.4	3.7	5.8	1	54.6	11.6

(a) 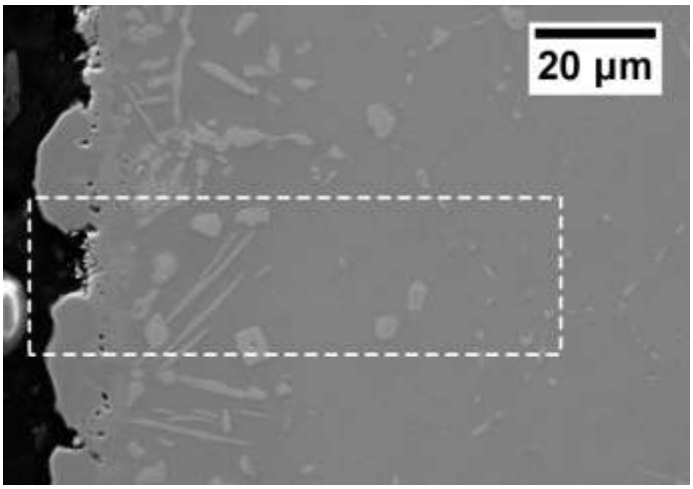

(b) 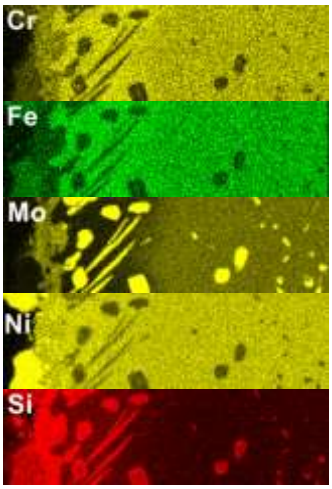

Figure 41. SEM cross-sectional micrographs and EDS elemental distribution of Hastelloy N sample system designated N-Na exposed to molten FLiNaK salt and metallic sodium at 850°C for 1000 hours.

Sample set N-Na, containing Hastelloy-N and FLiNaK salt for 1000 hours at 850°C, experienced the smallest weight change of all Hastelloy-N samples. Similar to all other Hastelloy-N results, the samples appear to have undergone an electrochemical plating process and associated species diffusion at the coating interface. Plan view SEM/EDS depicts several different morphologies, seen in Figure 40 and Table 9. Bulbous formations extending from the surface are rich in silicon and nickel, while the porous substrate shows high contents of silicon, nickel and molybdenum. The enriched silicon could have been derived from the Hastelloy-N substrate or may have been introduced into the stainless steel crucible system during an abrasive machining process.

As in the zirconium impact studies on Hastelloy-N, the interaction of Hastelloy-N with the stainless steel crucible makes it difficult to judge whether the sodium redox agent has a positive influence on the Hastelloy-N coupon. However, due to the electropositive nature of the major nickel alloy, it can actually give us insight into how the sodium redox agent impacts the stainless steel crucible. As shown in Figure 34 and Figure 36, corrosion products (Fe, Cr) derived

from the stainless steel crucible commonly electroplate through the salt onto the Hastelloy-N samples, creating Fe/Cr enriched layers. The SEM/EDS cross section shown in Figure 41 lacks a distinct Fe/Cr enrichment layer, suggesting that there is less free iron or chromium derived from the stainless steel crucible. This result suggests that sodium has a beneficial impact on limiting the corrosion of stainless steel.

SEM/EDS plan view analysis for samples designated N-Na-Gr, comprised of Hastelloy-N, sodium, and graphite in a 316L crucible heated for 1000 hours at 850°C can be seen in Figure 42 and Table 10.

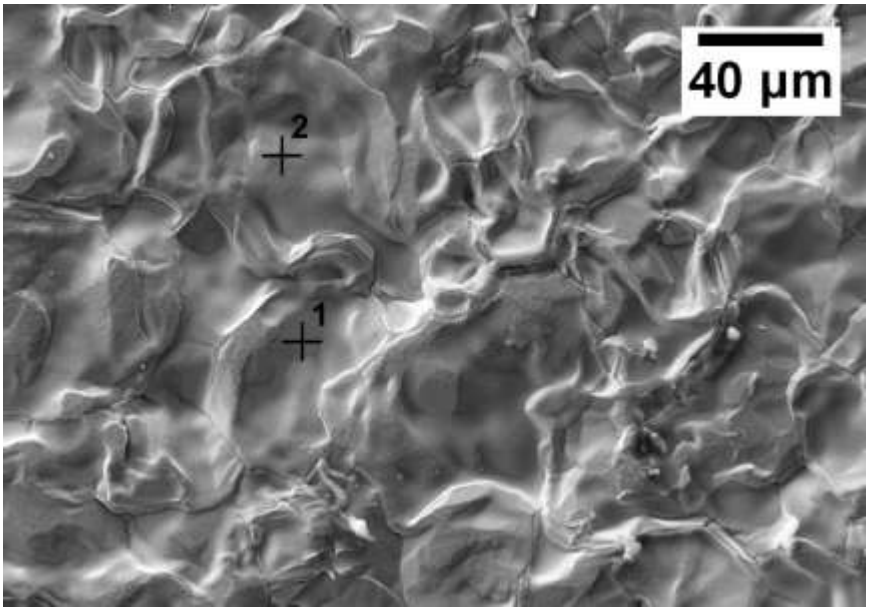

Figure 42. Plan view SEM micrograph of Hastelloy-N exposed to FLiNaK with sodium and graphite for 1000 hours at 850°C. Sample designation N-Na-Gr.

Table 10. EDS composition of several points taken from Hastelloy-N exposed to FLiNaK with metallic sodium and graphite for 1000 hours at 850°C.

Number	EDS Chemical Composition (at. %)						
	Al	Si	O	Cr	Fe	Ni	Cu
1	6.4	14.3	6.1	0.5	1.5	69.2	1.9
2	6.6	15.7	9.4	0.5	1.7	62.6	3.1

Plan view SEM/EDS data show a smooth surface comprised of Ni, Si, Al, and O. The large measured weight gain of these Hastelloy-N samples, combined with very little Fe, Cr, or Mo present, suggests the layer was formed through plating effects. The presence of Al and O is explained by the post processing steps to clean salt from the surface which involved dissolving the frozen FLiNaK salt in a bath of aluminum nitrate; therefore, Al and O were likely not present in large quantities during the corrosion process.

The frozen FLiNaK cross section is nearly identical in appearance to the system containing 316L stainless steel, seen in Figure 30b.

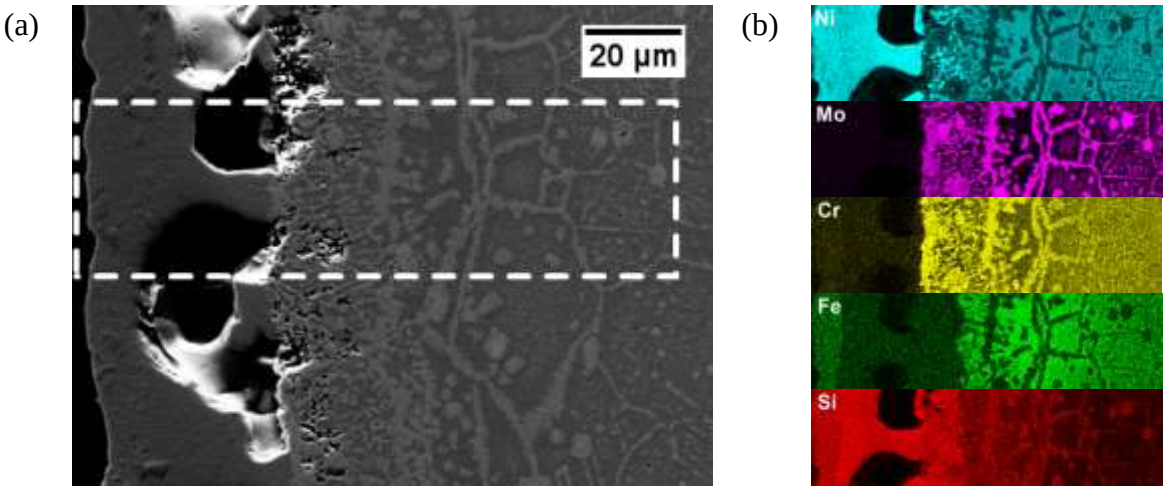

Figure 43. SEM cross-sectional micrographs and EDS distribution of Hastelloy-N sample system designated N-Na-Gr exposed to molten FLiNaK salt, metallic sodium, and graphite at 850°C for 1000 hours.

SEM cross section and EDS elemental distribution can be seen in Figure 43. Similar to systems containing zirconium, there is a thick plating layer characterized by nickel diffusion and near surface Cr and Mo phase instability. The coating is characterized by large gaps near the surface.

4.6 Hastelloy-N Transient Effects

To observe time dependent effects of Hastelloy-N corrosion in molten FLiNaK salt at 850°C, a single crucible was tested for an extended duration of 2000 hours (approximately 12 weeks). This crucible contained three Hastelloy-N samples with salt only, in a 316L crucible. By observing weight gain, conclusions can be drawn as to the rate nature of the corrosion process: linear vs. exponential vs. logarithmic.

Transient weigh change characteristics can be seen in Figure 44. The data indicate that an extended 2000 hour exposure results in a greater area specific weight gain for the Hastelloy-N coupons when compared with the 1000 hour exposure. As explained in earlier sections, this weight gain can be explained by electrochemical plating of species taken from the 316L crucible. However, this increased weight gain should not be taken as indication of increased attack on the 316L crucible. As shown in the transient analysis of 316L samples exposed to FLiNaK for 2000 hours, there is no significant increase in chromium depletion due to extended test duration. Therefore, the time-dependent increase in weight gain can be attributed to the kinetics of the plating process. Essentially, the salt can deplete species faster than the plating process can occur.

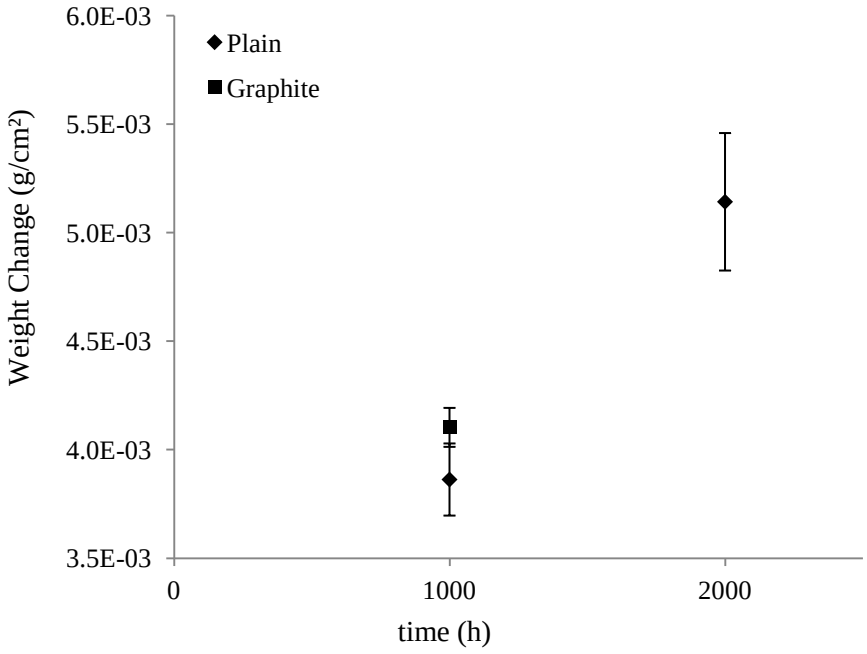

Figure 44. Weight comparison between static corrosion tests containing Hastelloy-N held at 850°C in FLiNaK molten salt for 1000 and 2000 hours.

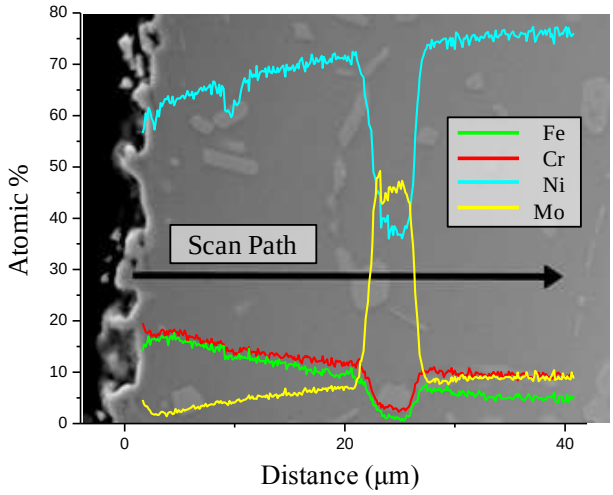

Figure 45. Cross-sectional SEM micrographs and corresponding EDS linescan analysis of Hastelloy-N tested without graphite in FLiNaK at 850°C for 2000 hours.

As can be seen in the SEM cross sectional image and corresponding EDS linescan, the Hastelloy-N sample exhibits a similar Fe/Cr/Ni rich deposit layer as described in Figure 34 and Figure 36. There are no new phase formations of differences in morphology of the plated layer.

4.6 Graphite

Graphite plays an important role in the nuclear industry. FHR and Generation IV reactor designs place nuclear grade graphite in critical roles where the material is expected to maintain geometry under high neutron flux, high temperature, and challenging chemical conditions [11]. Therefore it is necessary to understand how the material will behave when several materials are present in a high temperature molten salt system in order to identify potential operational issues in a full scale molten salt reactor system.

The graphite used in all tests of this present work is POCO Graphite grade AXF-5Q. This industrial grade graphite was selected due to its well characterized material properties and for its common use in other corrosion studies [68].

4.6.1 Carbide Alloying Effect

One phenomena pertaining to graphite in systems not containing a redox agent was an electrochemical alloying effect, where the graphite sample would emerge covered in a silver coating. For the 316L samples in contact with these graphite pieces, an increase in weight loss and chromium depletion was noticed. See section *4.2.1 Graphite Effect* for a description of the graphite effect on 316L.

(a)  (b) 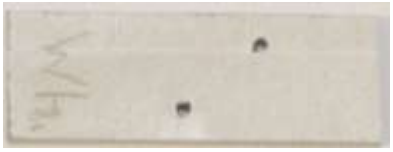

Figure 46. (a) Typical graphite coupon appearance prior to exposure to FLiNaK at 850°C for 1000 hours. (b) Graphite coupon after cleaning showing the presence of the chrome carbide coating. The length is shorter because a cross section of the sample has been taken.

(a)

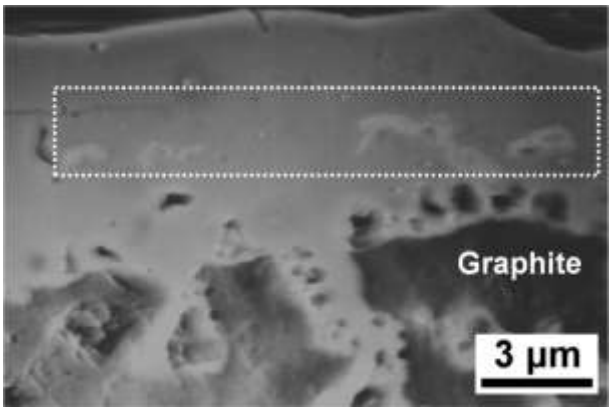

(b)

Figure 47. (a) Cross-sectional SEM micrograph of graphite coupon tested with 316L in FLiNaK at 850°C for 1000 hours. (b) EBSD phase distribution map of the white dotted rectangular area on SEM micrograph. Green and red phases represent Cr_7C_3 and Mo_2C, respectively. Coating on graphite sample was composed of major Cr_7C_3 and minor Mo_2C particles.

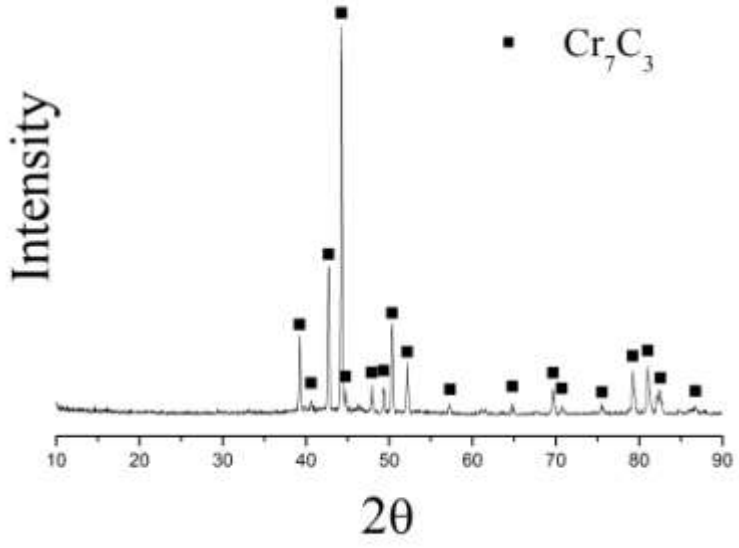

Figure 48. XRD analysis of graphite coupon tested with 316L in FLiNaK at 850°C for 1000 hours.

Figure 46 shows the change in visual characteristics of graphite samples tested with 316L. After exposure to FLiNaK at 850°C for 1000 hours, the graphite sample was covered with a silver coating; EDS analysis of the coating indicates the major constituent of the coating is Cr and a minor constituent is Fe (Cr:Fe at.% ratio is ~10). XRD indicates the coating on graphite is Cr_7C_3 carbide, as shown in Figure 48. Due to the Fe detected in the coating on graphite, the Cr_7C_3 revealed by XRD should modified as $(Cr,Fe)_7C_3$, in which Fe entered into solid solution in Cr_7C_3. Cross-sectional SEM micrograph of graphite samples (Figure 47) shows surface $(Cr,Fe)_7C_3$ formation approximately 10 μm thick.

Some bright particles were found in $(Cr,Fe)_7C_3$. EDS revealed these bright particles to be rich in Mo and Cr, as well as a few atomic % Fe (Mo:Cr:Fe at.% ratio is 7:3:1). Phase identification of the bright particles was carried out by EBSD due to the inability of EDS to provide accurate carbon measurement. EBSD phase distribution map of the $(Cr,Fe)_7C_3$ coating containing bright particles revealed that the bright particles are Mo_2C carbide as shown in Figure 47b. According to the EDS observation of the presence of Cr and Fe in Mo_2C carbide, Cr and Fe are considered to stay as solid solution form in Mo_2C. Thus, Mo_2C should modified as $(Mo,Cr,Fe)_2C$.

Previous molten FLiNaK static corrosion tests performed in graphite crucibles observed the formation of $(Cr,Fe)_7C_3$ on graphite [16]. However, Mo_2C was not noted to have been formed. It is possible that the Mo_2C was simply overlooked as the formations are small and blend well within the chrome carbide coating. The $(Cr,Fe)_7C_3$ plating process occurs through the nonelectric transfer of Cr and Fe from 316L to electropositive graphite as described by Ozeryanaya [69]. According to Ozeryanaya, electronegative metals would dissolve into the molten salt bath at low oxidation states (i.e. Cr^{2+} or Mo^{2+}) then undergo simultaneous oxidation

and reduction at the surface of the electropositive material, provided an alloy could be formed between the dissolved and electropositive species. An example of the carbiding process is shown in equation 5.

$$3Cr^{2+} \rightarrow 2Cr^{3+} + CrC_{carbide} \qquad (5)$$

This effect accelerated the dissolution of Cr and Fe contained in 316L when graphite is present, which had been reflected on its weight change result. The formation of small amounts of $(Mo,Cr,Fe)_2C$ on graphite implies Mo in the 316L sample and crucible would still be corroded by FLiNaK, however based on the fluoride formation free energy, Mo is nobler than Cr, Fe, and Ni in FLiNaK. Since Ni was not detected in the graphite coating and the fluoride formation free energy of Ni is more negative than Mo, the formation of $(Mo,Cr,Fe)_2C$ can be attributed to the same mechanism as $(Cr,Fe)_7C_3$, i.e. the nonelectric transfer of Mo from 316L to graphite.

4.6.2 Graphite Damage through Oxidation by Zirconium

In all systems where graphite was contained in conjunction with zirconium, the graphite piece was damaged and broken up into several pieces within the salt. According to Ozeryanaya's research of corrosion of Zr in molten chloride salt in glassy carbon crucible [70], finely dispersed ZrC particles have been observed in the salt. The formation of ZrC particles is caused by the galvanic effect between Zr and the glassy carbon crucible, resulting in the transfer of Zr through molten salt toward the more electropositive glassy carbon crucible. However, the ZrC particles dispersed in the salt implies that the cathodic glassy carbon would still be dissolved in the galvanic process. The same result was observed in our study. The graphite samples in 6-Zr-Gr and N-Zr-Gr crucibles have been dissolved and broken into pieces in the salt even though graphite acted as cathode in the Zr/graphite galvanic couple. On the other hand, it can be found that the number and size of the ZrO_2 crystals embedded in the coatings on 316L and Hastelloy-N

were much less when graphite was present in the salt. This result can be explained by the dissociation of ZrO_2. The process is as the following:

$$C + 4HF \rightarrow CF_4 + 2H_2 \quad (6)$$

$$ZrO_2 + CF_4 \rightarrow ZrF_4 + CO_2 \quad (7)$$

The graphite sample was initially corroded by HF, which was generated by the reaction of H_2O and salt, to form CF_4. The ZrO_2 crystals growing on the sample would be corroded by CF_4 and then generated CO_2 gas [71]. The porous surface of the coatings on 6-Zr-Gr and N-Zr-Gr samples can also indicate the formation of gaseous CO_2 released from the dissociation of ZrO_2. Another possible reason for reduced ZrO_2 formation is that the oxygen coming from H_2O contamination was consumed by the formation of CO or CO_2 due to the oxidation of graphite sample.

4.6.3 Graphite Damage through Alkali Intercalation

As a redox agent, 1.5g metallic sodium was added to several corrosion crucibles in order to observe its effect on alloy corrosion. Interestingly, metallic sodium had an even greater damaging effect on graphite than zirconium. Following the completion of the static corrosion tests containing sodium and graphite, no remaining graphite pieces were visible. Once crucible cross sections were taken, small black particles were found to be dispersed throughout the salt. It is suspected that these black particles are broken up graphite dispersed throughout the salt.

Figure 49. Graphite particle dispersion within frozen FLiNaK in a crucible containing 316L, graphite and metallic sodium held for 1000 hours at 850°C.

Due to the highly damaging effect of sodium on graphite, it is necessary to explore this mechanism further. The industrial production of aluminum through the Hall–Héroult process involves electrolysis of alumina dissolved in molten cryolite (Na_3AlF_6) [68, 72, 73]. The process requires the use of carbon cathodes which results in carbon exfoliation and damage through the undesirable uptake of sodium into the porous cathode surface [68]. Examining literature pertaining to this industrial process is a practical way to gain insight in the graphite degradation of the present work due to the shared fluoride salt chemistry and high operational temperature.

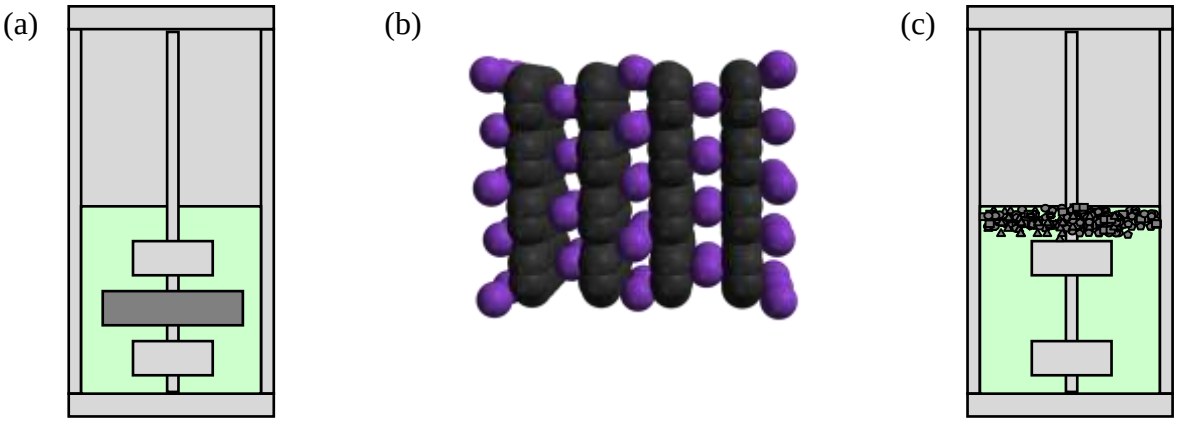

Figure 50. Graphite intercalation process by alkali metallics in molten FLiNaK. (a) Beginning of corrosion test. (b) Schematic of alkali uptake between layers of graphene. (c) Complete graphite erosion.

To understand the carbon anode degradation mechanics of the Hall–Héroult process, Adhoum et. al. performed an electrochemical characterization of graphite intercalation in molten NaF with metallic Na addition at 1025°C [68]. Intercalation is a reversible process where molecules are inserted between layers of other molecular structures. Coincidentally, Adhoum used POCO grade AXF-5Q graphite for the graphite electrode (the exact grade of graphite used in the present work). Through cyclic voltammetry techniques and x-ray diffraction analysis, it was shown that Na can successfully intercalate with the graphite electrode to cause interstitial expansion and eventual erosion.

In a similar study, D. Liu showed that a nearly identical process can occur in a system of metallic potassium dissolved in KF at 890°C [72, 73]. Although no metallic potassium was present in the test systems, potassium reduction is thermodynamically favorable as NaF is slightly more stable than KF. Such a reaction would occur until equilibrium is reached between KF, NaF, Na, K [74].

$$KF + Na = NaF + K \qquad (8)$$

The two processes of alkali intercalation explained by Adhoum and Liu are likely the cause of graphite degradation in the present work. Following eventual detachment of the graphite sample from the mounting rod, the broken up graphite likely floated to the top of the salt pool due to density effects, as shown in Figure 50.

An unintended consequence of the erosion process is that graphite undergoes an order of magnitude growth in surface area – akin to using graphite powder in the test instead of a solid graphite piece. Numerous effects in this galvanic system are highly sensitive to the surface areas of individual components, especially the carbide alloying effect described previously in this section. Some results suggest graphite intercalation in a FLiNaK system may have severe consequences for corrosion characteristics of 316L and Hastelloy-N. For a more thorough explanation of these effects, see the section regarding graphite effect on 316L.

4.6.4 Graphite Transient Effects

To study transient corrosion effect of stainless steel, a crucible containing 316L and a graphite sample was prepared and exposed to FLiNaK salt at 850°C for 2000 hours (1000 hours longer than the typical exposure duration in this work). As shown previously, the weight loss and resultant corrosive effects on 316L were not significantly larger than the results at 1000 hours. This is a beneficial result for 316L and suggests that corrosion is a short lived phenomenon under the testing conditions of this work.

However, the transient 316L results do not provide an indication of the kinetics behind the chrome carbide formation on graphite samples. It is important to have an idea how quickly this process occurs because this carbide formation can have consequences for FHR reactor designs. If the carbide forms a thin layer which does not grow over time then the formation may not be a big problem for reactor operators. Results from transient Hastelloy-N exposures suggest

electroplating kinetics are significantly different than the corrosion kinetics. Therefore it is necessary to examine transient exposure effect on graphite samples.

(a) 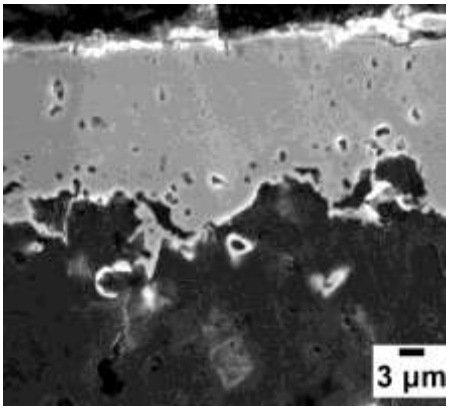

(b) 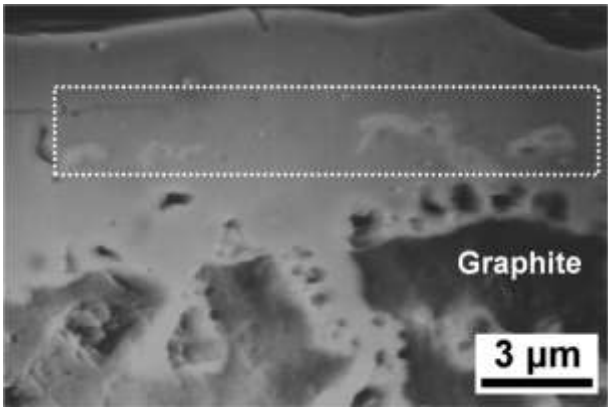

Figure 51. Cross-sectional SEM micrograph of graphite coupon tested with 316L in FLiNaK at 850°C for 2000 hours (a) compared against an equivalent system tested for 1000 hours (b).

4.7 Results Summary

4.7.1 Optical Salt Cross Sections

It has been observed that corrosion products are capable of changing the optical properties of molten FLiNaK salt; therefore it may be useful in some cases to observe the frozen color of the salt [20]. Darker salts are indicative of dissolved fluorine corrosion products and white salts may be indicative of containing less corrosion products. Salt cross sections are also useful in observing graphite effects, especially in the case of intercalation when sodium and graphite were in contact.

Table 11. Frozen salt cross sectional images for all 316L testing scenarios.

Table 12. Frozen salt cross sectional images for all Hastelloy-N testing scenarios.

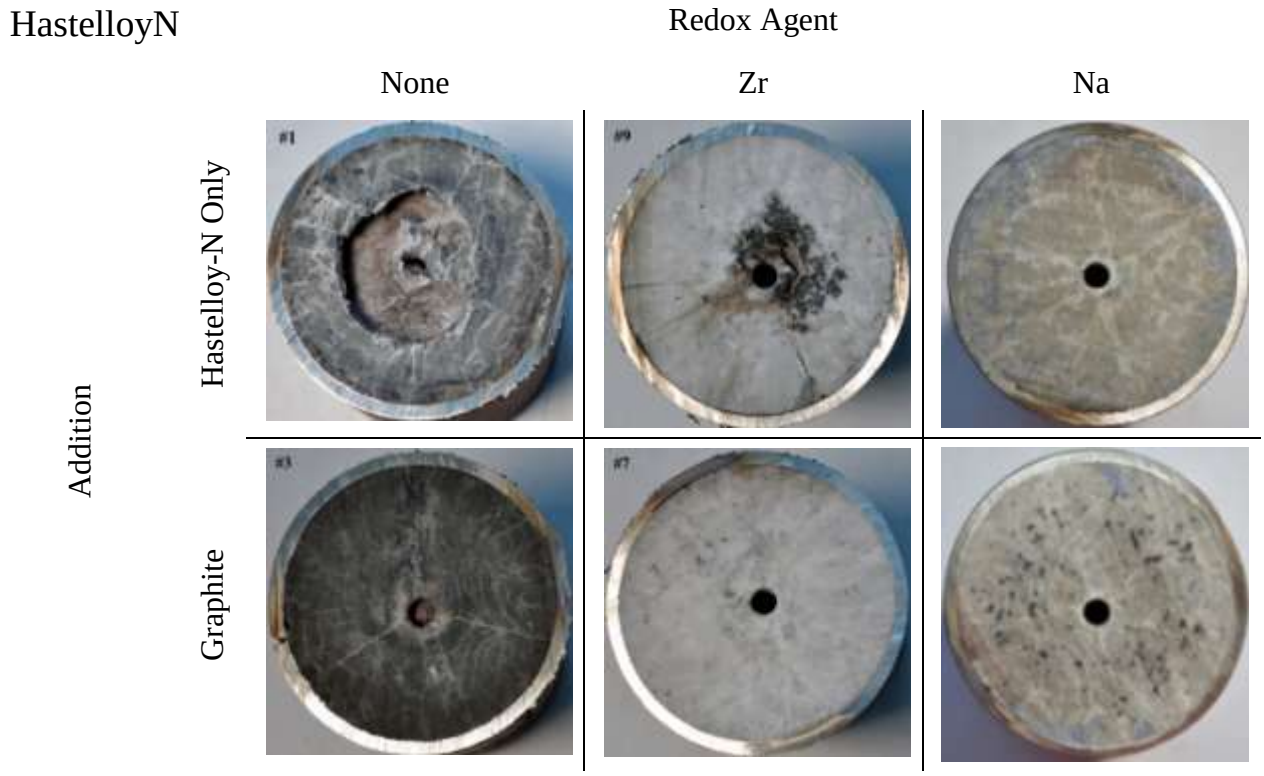

4.7.2 Summary of All Static Corrosion Test Results

The following table summarizes all corrosion results and material interactions effects for the designated material (316L, Hastelloy N, Graphite). All systems contained FLiNaK salt in a 316L crucible.

Material: 316L

Material additions	Designation	Test parameters	Notes
None	6-Plain	1000h, 850°C	• Weight loss due to slight surface chromium depletion up to 30 μm depth.
Graphite	6-Gr	1000h, 850°C	• Weight loss due to slight surface chromium depletion up to 50 μm depth accelerated by graphite alloying effect.
Zirconium	6-Zr	1000h, 850°C	• Weight gain due to thin Ni-Zr phase formation at surface caused by Zr electrochemical plating. Coating acted as chromium diffusion barrier.

Zirconium, Graphite	6-Zr-Gr	1000h, 850°C	• Weight gain due to thin Ni-Zr phase formation at surface caused by Zr electrochemical plating. Coating acted as chromium diffusion barrier. • CO_2 creation suspected to have caused porous coating structure.
Sodium	6-Na	1000h, 850°C	• Slight weight gain. • Phase instability and magnetization. • Chromium rich phases at surface.
Sodium, Graphite	6-Na-Gr	1000h, 850°C	• Surface instability and spallation. • Phase instability and heavy magnetization.
None	6-2000	2000h, 850°C	• No significant increase in weight loss and corrosion compared to sample set 6-Plain.
Graphite	6-Gr-2000	2000h, 850°C	• No significant increase in weight loss and corrosion compared to sample set 6-Gr-2000.

Material: Hastelloy N

Material additions	Designation	Test parameters	Notes
None	N-Plain	1000h, 850°C	• Weight gain due to Fe, Cr electroplating of corrosion products from 316L crucible.
Graphite	N-Gr	1000h, 850°C	• Weight gain due to Fe, Cr electroplating of corrosion products from 316L crucible.
Zirconium	N-Zr	1000h, 850°C	• ZrO_2 crystal formation and substrate dealloying caused by Zr electroplating and resultant Ni interdiffusion.
Zirconium, Graphite	N-Zr-Gr	1000h, 850°C	• Substrate dealloying caused by Zr electroplating and heavy Ni interdiffusion. • CO_2 creation suspected to have caused porous coating structure.
Sodium	N-Na	1000h, 850°C	• Thin plating layer with correspondingly small weight gain.
Sodium, Graphite	N-Na-Gr	1000h, 850°C	• Thick plating layer containing silicon and correspondingly high weight gain.
None	N-2000	2000h, 850°C	• Larger area specific weight gain caused by thicker electroplating due to longer exposure duration.

Material: Graphite

Material additions	Test parameters	Notes
None	1000h, 850°C	• Chrome carbide, molybdenum carbide phase formation at surface. • Sample appearance changed from black to silver.
Zirconium	1000h, 850°C	• Graphite damage due to carbon dioxide formation.
Sodium	1000h, 850°C	• Complete graphite erosion by sodium intercalation effect.
None	2000h, 850°C	• Thicker chrome carbide coating.

5 Conclusion

To utilize the advantageous thermo physical properties of molten fluoride salts for high temperature heat transfer applications, it is necessary to understand how the corrosive properties of these salts will affect several different structural alloys in a realistic reactor scenario containing a variety of nuclear materials. In addition, the effectiveness of using metallic redox agents to diminish molten salt corrosion must be evaluated. To gain insight into this corrosion process, static corrosion tests were conducted exposing structural alloys to molten LiF-NaF-KF under an assortment of chemical environments. These chemical environments simulated a realistic reactor scenario by placing structural alloys in contact with nuclear grade graphite as well as alongside potential reduction-oxidation materials.

All static corrosion tests were performed for 1000 to 2000 hours at 850°C in a 316L stainless steel crucible. In systems containing only 316L and salt, classic chromium depletion was observed near the surface of 316L stainless steel and effect accelerated by graphite carbide formation. Based on the results of transient tests, the classic chromium depletion corrosion process is likely an intense but short lived process driven by initial salt impurities and does not scale linearly with time. Both redox scenarios leave chromium protected relative to a system of only salt and alloy. However, sodium triggers near surface phase instability of 316L – an effect which merits further investigation. When graphite was placed with sodium, drastic and damaging phase instability was observed on 316L, resulting in heavy surface damage and spallation. It is theorized that granulated graphite induced carburization of 316L which led to chromium sensitization and segregation at grain boundaries.

Due to the nature of the test system, pure corrosion results of Hastelloy-N were clouded by galvanic driven species interaction. Zirconium is not a good material to use as a redox agent

in nickel based systems due to a high electromotive potential for plating between Zr and Ni, as well as a high interdiffusion coefficient between Ni and Zr . Damage to the Hastelloy-N samples was observed in the form of dealloying of nickel into zirconium rich plating layers. Sodium is a promising element, as minimal interactions were observed at the Hastelloy-N interface.

In real reactor environments, proximity of redox agent to graphite should be carefully considered. Combined with impurities present in the test system, zirconium caused damage to the graphite samples through CO_2 evolution. Sodium caused severe damage to graphite through intercalation, whereby sodium atoms induce interstitial expansion on graphene layers, leading to exfoliation and heavy damage.

Under the right chemistry, 316L is a viable container alloy for high temperature FLiNaK salt. If impurities can be minimized, there will be less attack on chromium and, as a result, less carbide formation on graphite. Precautions must be taken to effectively employ a redox agent. Results have shown that there is a damaging interaction between both zirconium, sodium. and graphite – so if redox is to be used, quantity and proximity to graphite must be carefully considered. Further work should be done to investigate pure corrosion of Hastelloy-N in environments free of interacting materials.

6 References

[1] J.H. DeVan, Effect of Alloying Additions on Corrosion Behavior of Nickel-Molybdenum Alloys in Fused Fluoride Mixtures. ORNL/TM-2021 (1969).

[2] Haynes International, HASTELLOY® N alloy. 2012.

[3] R.C. Briant, A.M. Weinberg, The Aircraft Reactor Experiment, *Nuclear Science and Engineering*. 2 (1957) 797.

[4] W.R. Grimes, D.R. Cuneo, F.F. Blakenship, G.W. Keilholtz, H.F. Poppendiek, M.T. Robinson, Chemical Aspects of Molten Fluoride Salt Reactor Fuels, in: Fluid-Fueled Reactors, Addison-Wesley, 1958, pp. 569.

[5] R.B. Briggs, Molten-Salt Reactor Program Semiannual Progress Report for Period Ending July 31, 1964. ORNL/TM-3708 (1964).

[6] A.M. Weinberg, The first nuclear era: the life and times of a technological fixer, Copernicus Books, 1994.

[7] H. MacPherson, The molten salt reactor adventure, *Nucl. Sci. Eng.* (1985).

[8] M.S. Sohal, M.A. Ebner, P. Sabharwall, P. Sharpe, Engineering Database of Liquid Salt Thermophysical and Thermochemical Properties. INL/EXT-10-18297 (2010).

[9] D.E. Holcomb, S.M. Cetiner, An Overview of Liquid-Fluoride-Salt Heat Transport Systems. ORNL/TM-2010/156 (2010).

[10] United States Department of Energy, A technology roadmap for generation IV nuclear energy systems. GIF-002-00 (2002).

[11] G.F. Flanagan, D.E. Holcomb, S.M. Cetiner, FHR Generic Design Criteria. ORNL/TM-2012/226 (2012).

[12] D.F. Williams, L.M. Toth, Chemical Considerations for the Selection of the Coolant for the Advanced High-Temperature Reactor. ORNL/GEN4/LTR-05-011 (2005).

[13] P.N. Haubenreich, J.R. Engel, Experience with the Molten-Salt Reactor Experiment, *Nuclear Applications and Technology*. 8 (1970) 118.

[14] D. Olander, Redox condition in molten fluoride salts Definition and control, *J. Nucl. Mater.* 300 (2002) 270-272.

[15] P. Calderoni, P. Sharpe, H. Nishimura, T. Terai, Control of molten salt corrosion of fusion structural materials by metallic beryllium, *J. Nucl. Mater.* 386-388 (2009) 1102-1106.

[16] L.C. Olson, J.W. Ambrosek, K. Sridharan, M.H. Anderson, T.R. Allen, Materials corrosion in molten LiF-NaF-KF salt, *J. Fluorine Chem.* 130 (2009) 67-73.

[17] L.C. Olson, Materials Corrosion in Molten LiF-NaF-KF salt. PhD Dissertation, University of Wisconsin-Madison (2009).

[18] L.C. Olson, J.W. Ambrosek, G. Cao, K. Sridharan, M.H. Anderson, T.R. Allen, Molten Salts for Nuclear Cogeneration, *Advances in materials science for environmental and nuclear technology*. 222 (2010) 145-156.

[19] L. Olson, K. Sridharan, M. Anderson, T. Allen, Nickel-plating for active metal dissolution resistance in molten fluoride salts, *J. Nucl. Mater.* 411 (2011) 51-59.

[20] J. Ambrosek, M. Anderson, K. Sridharan, T. Allen, Current status of knowledge of the fluoride salt (FLiNaK) heat transfer, *Nucl Technol*. 165 (2009) 166-173.

[21] J.W. Ambrosek, Molten Chloride Salts for Heat Transfer in Nuclear Systems. Doctor of Philosophy (Nuclear Engineering and Engineering Physics), University of Wisconsin-Madison (2011).

[22] M. Kondo, T. Nagasaka, Q. Xu, T. Muroga, A. Sagara, N. Noda, D. Ninomiya, M. Nagura, A. Suzuki, T. Terai, N. Fujii, Corrosion characteristics of reduced activation ferritic steel, JLF-1 (8.92Cr–2W) in molten salts Flibe and Flinak, *Fusion Eng. Des.* 84 (2009) 1081-1085.

[23] M. Kondo, T. Nagasaka, V. Tsisar, A. Sagara, T. Muroga, T. Watanabe, T. Oshima, Y. Yokoyama, H. Miyamoto, E. Nakamura, Corrosion of reduced activation ferritic martensitic steel JLF-1 in purified Flinak at static and flowing conditions, *Fusion Eng. Des.* 85 (2010) 1430-1436.

[24] A.K. Misra, J.D. Whittenberger, Fluoride salts and container materials for thermal energy storage applications in the temperature range 973 to 1400 K. Proceedings of the 22nd Intersociety Energy Conversion Engineering Conference cosponsored by the AIAA ANS ASME SAE IEEE ACS and AIChE, AIAA-87-9226, Philadelphia, PA (1987) 10-14.

[25] W.D. Manly, Metallurgical Problems in Molten Fluoride Systems, *Progress in Nuclear Energy*. 2 (1960) 164-179.

[26] ASM International, Corrosion by Molten Nitrates, Nitrites, and Fluorides. ASM Handbook Vol 13A: Corrosion: Fundamentals, Testing, and Protection (2003) 124-128.

[27] G.M. Adamson, R.S. Crouse, W.D. Manly, Interim report on corrosion by zirconium-base fluorides. ORNL/TM-2338 (1961).

[28] G.W. Mellors, S. Senderoff, Electrode Reactions in the Electrolysis of Fused Salts. Applications of Fundamental Thermodynamics to Metallurgical Processes - Proceedings of the First Conference on the Thermodynamic Properties of Materials held at the University of Pittsburgh. Pittsburgh, PA (1967) 81-103.

[29] J.R. Koger, Forced-convection loop corrosion studies. ORNL/TM-4832 (1973).

[30] R.B. Briggs, Molten-Salt Reactor Program Semiannual Progress Report for Period Ending February 28, 1962. ORNL/TM-3282 (1962).

[31] H. McKoy, R. Beatty, W. Cook, R. Gehlbach, C. Kennedy, J. Koger, A. Litman, C. Sessions, J. Weir, New Developments in Materials for Molten-Salt Reactors, *Nuclear Applications & Technology*. 8 (1970) 156-169.

[32] D. Williams, D. Wilson, L. Keiser, L.M. Toth, J. Caja, Research on Molten Fluorides as High Temperature Heat Transfer Agents (2003) 1-12.

[33] J.H. DeVan, R.B. Evans, Corrosion Behavior of Reactor Materials in Fluoride Salt Mixtures. ORNL/TM-328 (1962).

[34] R. Hurst, R.N. Lyon, Series IV: Technology, Engineering and Safety, Vol. 2, in: C.M. Nicholls (Ed.), Progress in Nuclear Energy, 1960, pp. 164-179.

[35] J.W. Koger, Alloy compatibility with LiF–BeF2 salts containing ThF4 and UF4. ORNL/TM-4286 (1972).

[36] L.E. McNeese, Molten-Salt Reactor Program Semiannual Progress Report for Period Ending August 31, 1975 (1976).

[37] J.R. Keiser, Compatibility studies of potential molten-salt breeder reactor materials in molten fluoride salts. ORNL/TM-5783 (1977).

[38] D.F. Williams, Assessment of candidate molten salt coolants for the NGNP/NHI Heat-Transfer Loop. ORNL/TM-2006/69 (2006).

[39] W.R. Grimes, Molten-Salt Reactor Chemistry, *Nuclear Applications & Technology*. 8 (1970) 137-155.

[40] J.H. Shaffer, Preparation and handing of salt mixtures for the molten salt reactor experiment. ORNL/TM-4616 (1971).

[41] W. Grimes, Chemical Research and Devlopment for Molten Salt Breeder Reactors. ORNL/TM-1853 (1967).

[42] R.B. Briggs, Molten-Salt Reactor Program: Semiannual Progress Report for Period Ending January 31, 1963. ORNL/TM-3419 (1963).

[43] R.B. Briggs, Molten-Salt Reactor Program Semiannual Progress Report for Period Ending July 31, 1963. ORNL/TM-3529 (1963).

[44] O. Beneš, R. Konings, 3.13 - Molten Salt Reactor Fuel and Coolant, *Comprehensive Nuclear Materials*. 3 (2012) 359-389.

[45] D. Williams, L. Toth, K. Clarno, Assessment of Candidate Molten Salt Coolants for the Advanced High-Temperature Reactor (AHTR). ORNL/TM-2006/12 (2006).

[46] J.R. Keiser, J.H. DeVan, D.L. Manning, The Corrosion Resistance of Type S16 Stainless Steel to Li_2BeF_4. ORNL/TM-5782 (1977).

[47] G.D. Del Cul, D.F. Williams, L.M. Toth, J. Caja, Redox Potential of Novel Electrochemical Buffers Useful for Corrosion Prevention in Molten Fluorides. Proceedings of the Thirteenth International Symposium on Molten Salts Held during the 201st meeting of the Electrochemical Society, Philadelphia, PA. (2002) 12-17.

[48] ASTM International, Standard Practice for Laboratory Immersion Corrosion Testing of Metals. G 31 - 72 (2004).

[49] NACE International, Standard Test Method - Laboratory Corrosion Testing of Metals. TM0169-2000 (2000).

[50] S.D. Cramer, B.S. Covino, Vol. 13A, Corrosion: Fundamentals, Testing, and Protection, ASM Handbook (2003).

[51] S. Evans, Correction for the effects of adventitious carbon overlayers in quantitative XPS analysis, *Surf. Interface Anal.* 25 (1997) 924-930.

[52] T.L. Barr, S. Seal, Nature of the use of adventitious carbon as a binding energy standard, *Journal of Vacuum Science & Technology A: Vacuum, Surfaces, and Films*. 13 (1995) 1239-1246.

[53] S.G. Hong, S.B. Lee, The tensile and low-cycle fatigue behavior of cold worked 316L stainless steel: influence of dynamic strain aging, *Int. J. Fatigue*. 26 (2004) 899-910.

[54] ASME, *Boiler & Pressure Vessel Code Section III* Rules for Construction of Nuclear Facility Components - *Division 1:* Subsection NH - Class 1 Components in Elevated Temperature Service (2007).

[55] L. Olson, J. Ambrosek, K. Sridharan, M. Anderson, T. Allen, M. Corradini, Evaluation of Material Corrosion in Molten Fluoride Salt. Proceedings of the American Institute of Chemical Engineering Annual Meeting and Fall Showcase, (2006) 12-17.

[56] POCO Incorporated, AXF-5Q. 2012.

[57] B. Kelleher, R.S. Sellers, M.H. Anderson, K. Sridharan, R.D. Scheele, Chemistry Control and Corrosion Mitigation of Heat Transfer Salts for the Fluoride Salt Reactor (FHR).

International Conference on Advances in Nuclear Power Plants (ICAPP 2012), Chicago, Illinois (2012).

[58] D. Ludwig, Analysis Techniques for Corrosion Product Detection in Molten Salts: High Temperature Electrochemistry and Neutron Activation Analysis. Masters of Science in Nuclear Engineering and Engineering Physics, University of Wisconsin-Madison (2008).

[59] B. Weiss, R. Stickler, Phase instabilities during high temperature exposure of 316 austenitic stainless steel, *Metallurgical and Materials Transactions B*. 3 (1972) 851-866.

[60] V. Raghavan, The Fe-Ni-Zr (Iron-Nickel-Zirconium) System, Phase Diagrams Ternary Iron Alloys, *Indian Inst. Met.* 6B (1992) 1094-1098.

[61] D.B. Abraham, J.W. Richardson, S.M. Mc Deavitt, Microscopy and neutron diffraction study of a zirconium-8 wt% stainless steel alloy, *Journal of Material Science*. 36 (2001) 5143-5154.

[62] G. Ghosh, Thermodynamics and kinetics of stable and metastable phases in the Ni–Zr system, *J. Mater. Res.* 9 (1994) 598-616.

[63] C. Wang, M. Zinkevich, F. Aldinger, On the thermodynamic modeling of the Zr–O system, *Calphad*. 28 (2004) 281-292.

[64] Y. Zhang, B.A. Pint, G.W. Garner, K.M. Cooley, J.A. Haynes, Effect of cycle length on the oxidation performance of iron aluminide coatings, *Surface and Coatings Technology*. 188 (2004) 35-40.

[65] J. Golczewski, H.L. Lukas, M. Bamberger, S.F. Dirnfeld, Phase Diagrams of the Ni-Fe-Mo and Ni-Cr-Mo Ternary Systems--Experiments and Thermodynamic Calculations as a Basis of Superalloy Development. Advanced Materials and Processes - Proceedings of the First European Conference. EUROMAT'89. Aachen, Germany. 1 (1989) 365-370.

[66] G. Ghosh, Aluminium-Nickel-Zirconium, in: Ternary Alloys, Wiley-VCH, 1992, pp. 71-78.

[67] Y.V. Voroshilov, V.Y. Markiv, E. Gladyshevskii, The Zirconium-Nickel-Silicon System (1967) 1228.

[68] N. Adhoum, J. Bouteillon, D. Dumas, J.C. Poignet, Electrochemical insertion of sodium into graphite in molten sodium fluoride at 1025 °C, *Electrochim. Acta*. 51 (2006) 5402-5406.

[69] I.N. Ozeryanaya, Corrosion of metals by molten salts in heat-treatment processes, *Metal Science and Heat Treatment*. 3 (1985) 184-188.

[70] I.N. Ozeryanaya, V. Tkhai, M.V. Smirnov, E.A. Burakova, Effect of container material on reaction of zirconium with molten strontium chloride, *Tr. Inst. Elektrokhim., Ural. Nauch. Tsentr. Akad. Nauk SSSR* (1973) 86-89.

[71] D. Devilliers, M. Vogler, F. Lantelme, M. Chemla, Mass spectrometric analysis of thermal decomposition products of graphite fluorides and electrogenerated carbon--fluorine compounds, *Anal. Chim. Acta*. 153 (1983) 69-82.

[72] D. LIU, W. LI, Z. YANG, S. QIU, Y. LUO, Electrochemical investigation on kinetics of potassium intercalating into graphite in KF melt, *Transactions of Nonferrous Metals Society of China*. 21 (2011) 166-172.

[73] D. Liu, Z. Yang, W. Li, S. Qiu, Y. Luo, Electrochemical intercalation of potassium into graphite in KF melt, *Electrochim. Acta*. 55 (2010) 1013-1018.

[74] B. Laurenty, The LM-LS experiment: investigating corrosion control, in Liquid Fluoride Salts, by Liquid alkali Metal. Masters Thesis, University of California-Berkeley (2006).

[75] R.S. Sellers, B. Kelleher, W.J. Cheng, K. Sridharan, M.H. Anderson, T.R. Allen, Materials corrosion in molten LiF-NaF-KF eutectic salt under different reduction-oxidation conditions. International Conference on Advances in Nuclear Power Plants (ICAPP 2012), Chicago, Illinois (2012).

[76] K. Knox, D.W. Mitchell, The preparation and structure of K2NaCrF6, K2NaFeF6 and K2NaGaF6, *Journal of Inorganic and Nuclear Chemistry*. 21 (1961) 253-258.

[77] K.H. Stern, M.E. McCollum, Electrodeposition of silicon from molten salts, *Thin Solid Films*. 124 (1985) 129-134.

[78] D. Elwell, Electrowinning of silicon from solutions of silica in alkali metal fluoride/alkaline earth fluoride eutectics, *Solar Energy Materials*. 5 (1981) 205-210.

[79] A.L. Bieber, L. Massot, M. Gibilaro, L. Cassayre, P. Chamelot, P. Taxil, Fluoroacidity evaluation in molten salts, *Electrochim. Acta*. 56 (2011) 5022-5027.

[80] A.L. Bieber, L. Massot, M. Gibilaro, L. Cassayre, P. Taxil, P. Chamelot, Silicon electrodeposition in molten fluorides, *Electrochimica Acta*. 62 (2012) 282-289.

[81] M.T. Kim, J.S. Jung, Codeposition of Al and Si onto a low carbon steel using silicon dioxide and aluminum and its hot temperature oxidation properties, *Surface and Coatings Technology*. 161 (2002) 218-223.

[82] M. Fukumoto, C. Tachikawame, Y. Matsuzaka, M. Hara, Formation of Si diffusion layer on stainless steels and their high temperature corrosion resistance in molten salt, *Corros. Sci.* 56 (2012) 105-113.

[83] H. Hsu, W. Tsai, High temperature corrosion behavior of siliconized 310 stainless steel, *Mater. Chem. Phys.* 64 (2000) 147-155.

[84] K. Tatemoto, Y. Ono, R.O. Suzuki, Silicide coating on refractory metals in molten salt, *Journal of Physics and Chemistry of Solids*. 66 (2005) 526-529.

[85] R. Kent, J.L. Margrave, Mass Spectometric at High Temperatures. VIII. The Sublimation Pressure of Iron(II) Fluoride, *Journal of the American Chemical Society*. 87 (1965) 4754-4756.

7 Appendix

A. Test Failure

A.1 Experimental

High temperature systems containing fluoride salts commonly require substantial insulation to prevent accidental freezing and to minimize trace heat. However, little effort has been directed towards studying the interaction between fluoride salts and common insulation materials, which can occur in the event of a leak or failure. Therefore, very little is known how insulation introduced to a fluoride salt environment will impact the corrosion of structural materials.

In the present study, the failure of a 316L stainless steel crucible containing FLiNaK molten salt and subsequent interaction with furnace materials will be examined. Visual inspection, scanning electron microscopy (SEM) equipped with energy dispersive x-ray spectroscopy (EDS), and X-ray diffraction (XRD) analysis are carried out to identify the root cause of the system failure and understand the molten salt interactions with the furnace insulation material.

The original purpose of the experiment was to create a controlled test environment to study the static corrosion characteristics of clean molten FLiNaK on structural materials. The test consisted of nine crucibles constructed of 316L stainless steel tube with wall thickness approximately 3mm, welded shut on both ends and containing 512g FLiNaK. Installed in each crucible were several alloy test coupons upon which analysis would be performed at the conclusion of the test.

Salt preparation, crucible filling, and final welding was performed in a dry argon atmosphere glove box. At the testing temperature of 850°C, each sealed crucible would become pressurized to an extent corresponding to the initial quantity of argon contained in each crucible. Previous static corrosion tests have been fabricated and tested in the same manner with a successful outcome [16, 75].

A.2 Corrosion Characterization

Visual Observation

Figure 52. Photograph of crucibles at the conclusion of the 1000 hour static test.

(a) (b)

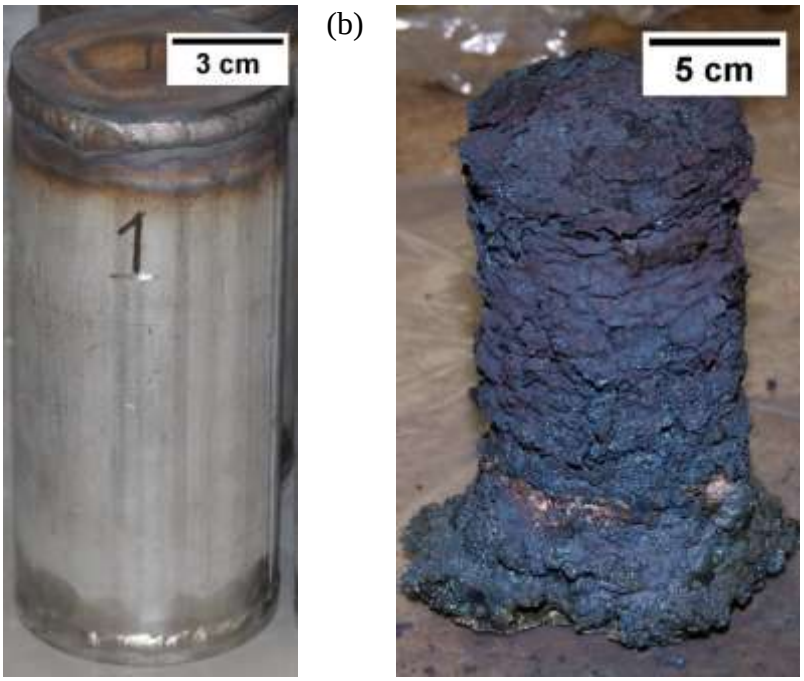

Figure 53. A comparison of a crucible (a) before corrosion test and (b) after corrosion test. There was substantial height and radial growth of the scale.

Figure 52 shows visual characteristics of the crucibles and the high temperature electric box furnace after the termination of the test. A close up comparison of a corroded crucible and a crucible prior to testing is shown in Figure 53. The scale formation is porous and brittle with shiny metallic sections and areas of green, white, purple, and red residue. The crucible interiors show relatively thin, predominately red, scale formations. Two steel sheathed type K thermocouples were used to monitor the internal temperature. Both were non operational, due to heavy corrosion, at the conclusions of the 1000 hour test. The alumina sheathed type S control thermocouple remained operational the entire time and appeared unaffected. Throughout the duration of the test, the furnace was held at slight positive pressure with nitrogen cover gas making oxygen ingress unlikely.

Figure 54. Cross section of the clay bonded SiC base plate used in the high temperature furnace. Affected areas are discolored black with some associated swelling.

The furnace base plate, constructed of 1mm sized particles of silicon carbide held in a clay matrix, showed extensive attack. The clay matrix is composed of minerals containing O, Si and Al. A cross section of the base plate can be seen in Figure 54 where affected areas are discolored black. The black damaged region is accompanied by light swelling, indicative of vapor formation.

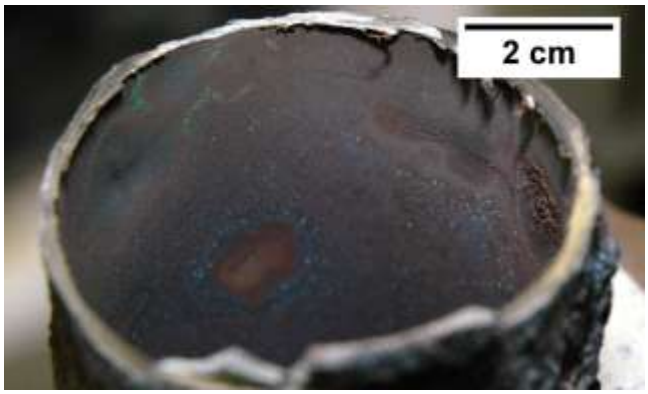

Figure 55. Circumferentially aligned stress cracking on the interior of one of the static test crucibles.

Figure 56. Point of failure located on the bottom weld.

Upon inspection, it appears that the set of nine static test crucibles failed by several different mechanisms. Some crucibles exhibit circumferential cracking, shown in Figure 55. Localized outward plastic deformation near the cracks indicates that they are stress induced. It is likely that these stress ruptures are the result of reduced crucible structural integrity caused by

outward corrosion combined with internal pressurization of the argon cover gas contained within the sealed crucible. It has been shown that a structurally sound crucible is able to contain this minor pressurization; therefore, since this failure mode depends on the presence of corrosive vapor, stress induced cracking cannot be the method by which FLiNaK was first released into the furnace [75]. One crucible, shown in Figure 56, has a prominent failure point located at a weld joint; therefore, a faulty weld with a pinhole leak is likely the mechanism by which FLiNaK initially escaped into the furnace.

SEM/EDS/XRD Characterization

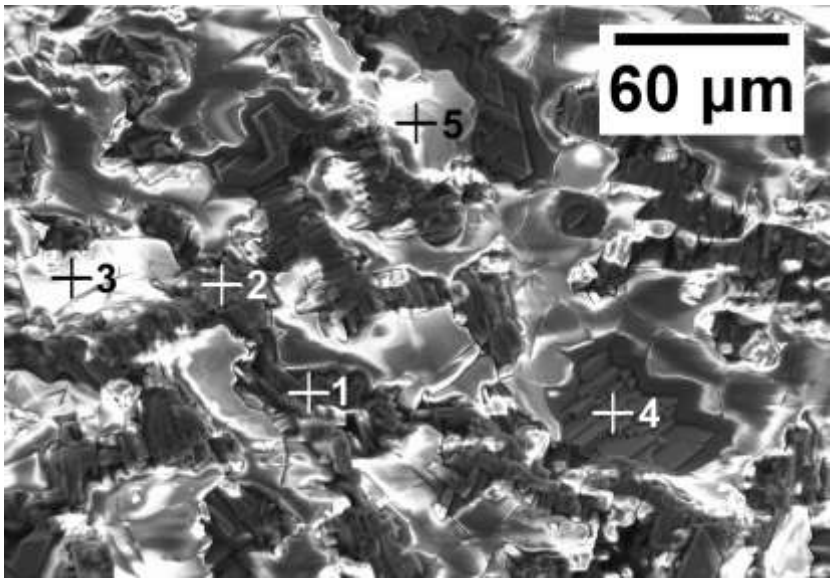

Figure 57. SEM micrograph of scale topology.

Table 13. EDS elemental distribution of scale topology.

Number	EDS Chemical Composition (at. %)					
	O	Al	Si	K	Cr	Fe
1	58.8	2.2	14.0	12.2	0.5	12.2
2	61.4	2.2	13.0	11.0	0.7	11.4
3	67.5	-	-	21.3	10.6	0.5
4	63.3	-	-	1.0	0.6	33.6
5	63.6	-	-	23.3	11.9	1.1

To understand the nature of the test failure, samples of corrosion crust from the top of a crucible were evaluated using SEM/EDS. Pieces taken from the top of the corroded crucibles display a variety of morphologies. Figure 57 shows jagged, rough sections found to be rich in O, Si, K, and Fe dispersed among smoother sections composed primarily of O, K, and Cr. Mixed within the jagged sections are points containing only Fe and O, identified as α-Fe_3O_3 (hematite). Cross section SEM/EDS maps and point scans of the crucible wall are shown in Figure 58 and Table 14. Depletion of iron and chromium along grain boundaries, starting at the crucible exterior and moving radially inwards, appears to be the main mode of attack. EDS point scans identify the F, Na, K rich compound existing between the grains as K_2NaCrF_6. XRD analysis of green substance present on the interior of the corroded crucibles provides positive identification of the presence of K_2NaCrF_6 in the test system as shown in Figure 59. The distinct emerald green color and x-ray pattern is consistent with the description of K_2NaCrF_6 synthesized and characterized by Knox [76].

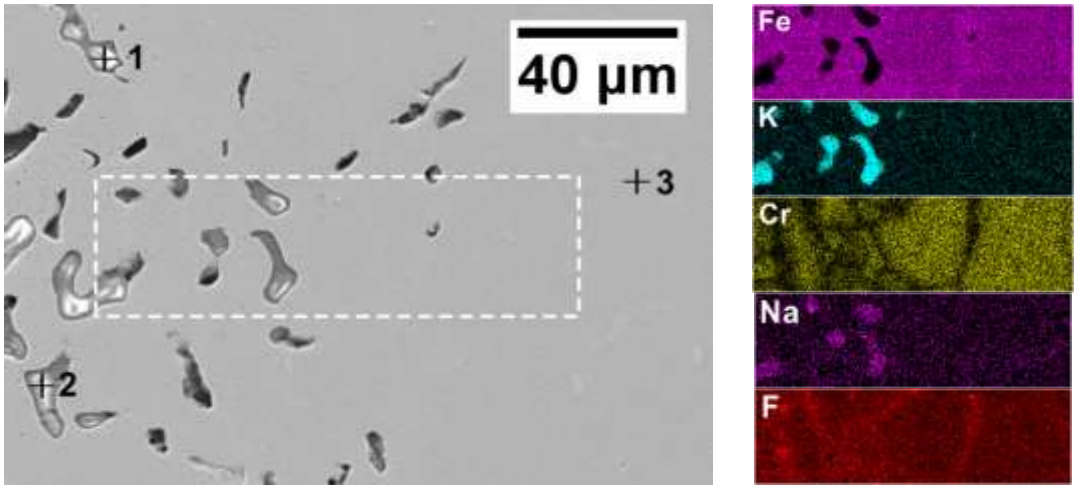

Figure 58. SEM micrograph of a crucible wall cross section with the corresponding EDS map elemental distribution.

Table 14. Point scan elemental distribution of a crucible wall cross section.

Number	EDS Chemical Composition (at. %)									Identification
	F	Na	Si	K	Cr	Mn	Fe	Ni	Mo	
1	62.7	9.8	-	17.5	9.0	-	0.8	-	-	K_2NaCrF_6
2	59.2	10.2	-	19.7	10.1	-	0.8	-	-	K_2NaCrF_6
3	-	-	1.4	-	18.0	1.9	67.6	10.3	0.9	γ (Fe,Ni)

EDS detection of F, Si, Na, and K on the top of the corroded crucible suggests the elements existed in vapor form at the testing temperature of 850°C. These elements are abundant in the system in either solid or liquid phases in the form of clay bonded SiC and molten FLiNaK salt, respectively. Thus, a reaction occurred between the molten salt and furnace insulation materials which lead to the creation of a corrosive vapor. Large quantities of oxygen were detected on the surface crust. However, oxygen was not present in large quantities in the system at testing conditions, so was likely introduced at the conclusion of the test when the furnace was opened to atmospheric air. Prior to opening the furnace, the temperature was allowed to cool to approximately 250°C. This could be a sufficiently high temperature to allow some surface oxidation. Further evidence that oxygen reactions were an isolated surface phenomenon is backed up by the lack of detected oxygen in the SEM/EDS cross sectional images of Figure 58. Therefore, oxygen was not a contributing factor to the failure of the system.

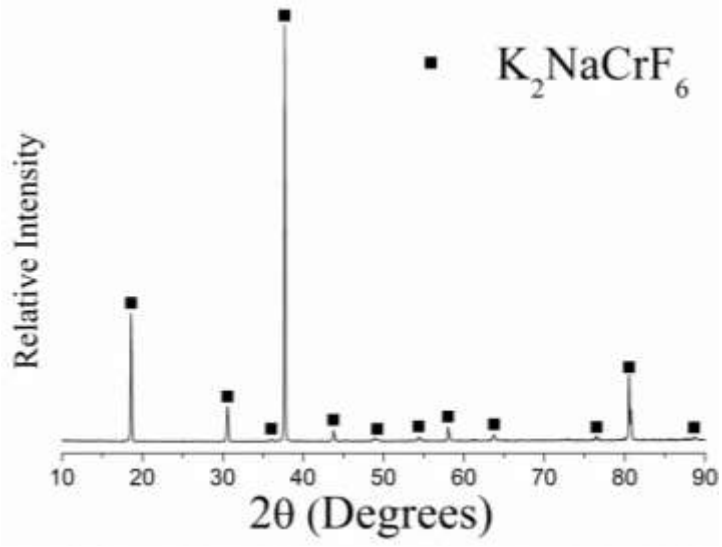

Figure 59. X-Ray diffraction pattern of green material recovered from the crucible.

A.3 Discussion

The test failure was likely initiated by a pinhole leak in a single crucible which allowed FLiNaK to escape and react with the clay bonded silicon carbide furnace base plate. The reaction taking place at 850°C created corrosive vapors of SiF_3, F_2, Na_2SiF_6, and K_2SiF_6, evident through the migration of initially solid or liquid phase elements (Si, F, Na, K) to the exterior of the 316L stainless steel crucibles and to the surface of steel sheathed thermocouples positioned above the crucible set. Investigation of the identity of these destructive vapors is pertinent, although precise identification of the vapors is made difficult by the complicated nature of the failure and subsequent material interaction.

Fluoride salts are a convenient medium for electrodeposition, especially in silicon containing systems [77-80]. In addition, fluoride salts and silicon compounds have been studied as pack cementation materials for the creation of steel coatings [81-84]. Therefore, the test results for the aforementioned studies are useful in understanding the present work because similarities in materials.

Of particular significance is a study performed by Elwell [78] where silicon was electrodeposited from solutions of SiO_2 and fluoride salt eutectics at high temperatures. In measuring the solubility of SiO_2 in various fluoride salt mixtures, it was noted that several mixtures produced volatile products at high temperatures. In particular, Na_2SiF_6 condensate was identified through XRD in NaF/MgF_2 and NaF/CaF_2 melts held at 1000-1100°C. K_2SiF_6 was thought to evaporate from mixtures containing KF. It is possible that these two vapors were created in the present study through an interaction of KF and NaF with the clay bonded silicon carbide furnace materials.

Fukumoto [82] described a pack cementation process for creating a silicon rich layer in SUS430 and SUS304. Silicon containing diffusion layer was observed in alloy samples covered in Si, SiO_2 and NaF powder mixture held for 24 hours at 950°C. Considering the similarities between SUS304 and 316L stainless steel, it is likely such a process could occur in the present study. Silicon transport into the metallic matrix can occur by equations 9-11.

$$12NaF(g) + 15SiO_2(s) + Si(s) = 6Na_2Si_2O_5(l) + 4SiF_3(g) \quad (9)$$

$$SiF_3(g) + M = Si(s) + MF_3(g) \quad (10)$$

$$SiF_3(g) + 2M = 2Si(s) + 2MF_2(g) + F_2(g) \quad (11)$$

M: Metal element (Fe, Cr, Ni)

Initially, a silicon fluoride vapor is formed between silicon oxide and sodium fluoride (equation 9) and proceeds to comes in contact with the alloy surface (equation 10). Continuing the reaction, metal fluoride compounds along with fluorine gas is formed and solid silicon is liberated at the alloy surface (equation 11) and is able to diffuse into the steel, leading to the

formation of the Si rich layer. In the Fukumoto paper [82], the chemical reactions were explained using thermodynamic calculations as well as XRD identification of the $6Na_2Si_2O_5$.

A similar process likely occurred in the present study due to the abundant supply of NaF, SiO_2 and Si contained in the box furnace system at high temperatures. Equation 12 is hypothesized as an explanation for the formation of K_2NaCrF_6 taking into account the process described by Fukumoto along with the K_2SiF_6/Na_2SiF_6 vapors shown to have been created in similar experimental systems. Such a reaction would also provide additional silicon fluoride vapor near the alloy surface to continue the fluorination process described by Fukumoto in equation 10-11.

$$2Na_2SiF_6(g) + 4K_2SiF_6(g) + 4Cr(s) + 3F_2(g) = 4K_2NaCrF_6(s) + 6SiF_3(g) \quad (12)$$

The formation of metallic fluorine compounds described by Fukumoto is consistent with the attack seen in the EDS cross sectional image of Figure 58, where depletion of chromium and iron can be observed. Previous work has shown that chromium and iron are the most thermodynamically favored alloying constituents for fluorine attack in a 316L stainless steel system [16]. In addition, it has been shown that Iron (II) Fluoride can sublimate at temperatures as low as 690°C [85]. Such a sublimation process explains the distinct iron voids in Figure 58 as well as the porous structure of the corrosion crust whereby Iron (II) fluorine vapor pockets would exert pressure on surrounding material, causing expansion and eventual release of FeF_2 vapor. Combining the Fukumoto silicon fluoride diffusion theory with the sublimation of FeF_2 and the synergistic effects of the K_2SiF_6/Na_2SiF_6 vapors over hundreds of hours, it can be seen how this processes would create a porous corrosion crust that compromises the structural integrity of the stainless steel tube.

A.4 Conclusion

Visual inspection, SEM/EDS examination, and XRD analysis were carried out to investigate the failure of a 316L stainless steel molten fluoride salt containing system in a high temperature box furnace held at 850°C for 1000 hours. It was found that FLiNaK molten salt escaped through a pinhole leak in a single static test crucible and reacted with the clay bonded silicon carbide base plate installed in the box furnace. Vapors of SiF_3, Na_2SiF_6, and K_2SiF_6 were formed and subsequently attacked the 316L system through a fluorination process described by Fukumoto and Elwell. It is hypothesized that this process contributed to the creation of K_2NaCrF_6 identified by XRD as well as the sublimation of FeF_2. These combined effects extended over hundreds of hours created a porous corrosion crust which caused the remaining static test crucibles to become structurally unsound. The compromised crucibles released additional FLiNaK contents which continued the vapor corrosion process.

A.5 Recommendations

Considering the large quantity of insulation typically found in systems containing heated molten salt and the destructive nature of the resulting corrosive vapors, some recommendations to minimize future corrosion failures are as follows:

1. Construct a stainless steel boat or perform the test in a retort furnace so leaked salt will only come into contact with metallic components. Such interactions are fairly well understood and vapors will not be created.
2. Minimize internal pressurization of static test crucibles through hot finish welding or vacuum sealing.
3. Verify weld integrity through x-ray analysis.

4. Construct a static test system with an independent heating system so system integrity can be verified without cooling and opening a furnace.

B. Static Test Procedure and Safety

Introduction

This guide is an overview of any hazards which will be faced during fabrication, testing and post processing of a molten FLiNaK salt static corrosion test. The static corrosion test, from start to finish, is broken up into six general sections. Within each section, tasks are outlined and a brief description of any safety hazards is included. Most sections include a description of personal protective equipment (PPE) required to carry out the task. Additional information is provided for the moist environment static corrosion test. This safety outline is not intended to be a procedural outline for a molten FLiNaK salt static corrosion test, nor does it apply for static corrosion tests performed in salts other than FLiNaK.

B.1 Crucible Fabrication

1.1 Raw material handing	Raw materials for the construction of the corrosion testing crucibles will come in a variety of forms, including 20 ft. lengths of pipe, long rods of small diameter and large sheets of steel. Long pipe and heavy stock present a safety hazard through finger pinching, accidental dropping on feet and can be cumbersome to move. If a certain piece is too large to move safely on one's own, find another person to help.
1.2 PPE	When in the shop, long pants, close toe shoes and safety glasses must be worn at all times. In addition, when operating large machines (saws, mill, lathe) one other person must be present in the shop in case of an emergency.
1.3 Machining – Pipe cutting	Care must be taken to align and properly support the pipe which is to be cut in the vertical band saw. Operator must receive proper training on the usage of the vertical band saw prior to use. Saw has the potential to grab any loose clothing or hair, so loose articles need to be tied back. Improper usage of the saw can result in the blade breaking which may create flying shrapnel.
1.4 Machining – Lathe	Use of the lathe presents several safety issues. 1. Proper training to know general usage is required. This includes proper tool and speed selection, correct ways to mount materials and use of lubricant. 2. Chips are never to be grabbed while the machine is turning. 3. Loose clothing or accessories must be tied back as to avoid getting caught in the spinning chuck during operation.
1.5 Machining – Mill	The mill presents many of the same safety hazards as the lathe. Proper training is required.

1.6 Machining – Grinding	Grinding material edges to remove burrs or sharp corners has the tendency to produce many small fast moving particles. These particles have the potential to enter the eye or cause cuts. Move at a slow pace and do not attempt to grind a large section of material at once.
1.7 Welding	Welding should only be performed by an experienced individual – usually Paul Brooks, Mark Anderson or Bryan Coddington.
1.8 Oakite solvent bath	Oakite is an acid used to dissolve oils and residue left on machined parts. To be used effectively, it must be heated to around 100F. The Oakite bath presents a low risk of heat and chemical burn through accidental splashing. If contact is made with skin, wash the area with water.
1.9 Sample polishing	Sample coupon batches must be polished through successive grinding until a fine grit is achieved. The polishing machine spins very rapidly and has the potential of grabbing any loose clothing. Like the shop, when in the basement CAE material-prep lab another person must be present to aid in the case of an emergency. The doors to this lab must remain open when lab is in use.
1.10 Final welding	Final welding will occur in an inert atmosphere glove box by a qualified and experienced person, usually Paul Brooks.

B.2 Salt Production

2.1 PPE	Personal protective equipment for the safe handling of salt includes: Saftety glasses, close toe shoes, long pants and gloves.
2.2 Chemical handing	Component salts for the production of the eutectic salt mixtures pose a low health hazard if accidentally spilled on exposed skin or eyes. According to Alfa-Aesar, in the event of exposure to skin or eyes, rinse immediately with water and seek medical advice. This safety advice only applies to the components and production of FLiNaK salt.
2.3 Heater operation (in glove box)	The salt heating and melting system installed in the glove box poses risk of burn and electrocution. When setting up the heater or modifying the position, be sure that power is not on. Watch for any uninsulated leads. (See Brian Kelleher's safety guidelines for glove box usage.) Burn risks still exist even through rubber glove box gloves. When heater is at high temperature only make indirect contact through the use of tongs or other means. When cutting power, allow adequate time for the heater to cool before touching.
2.4 Heater operation (outside of glove box)	If salt mixture is to be produced outside of the glove box, there are several additional safety issues. The risk of electrocution is heightened by the fact live leads can make direct contact with skin. Take precautionary measures to eliminate the risk of contact with live leads. During the heating and melting process, there is the potential for toxic fumes to be produced through salt reacting with water. If salt is to be produced outside of a glove box, it **must** be done under an operational hood.
2.5 Salt post production	After the salt cools and solidifies, it will need to be broken into pieces in the glove box by hand. Accidental injury can be incurred through improper use of the hammer and chisel. The break up process can be physically demanding, so move at a slower pace and take needed breaks.

B.3 Furnace Usage

3.1 Furnace power controls	To operate, the 240V breaker near the furnace needs to be in the

	‘on’ position. Check the area for any loose or disconnected wires extending from the breaker to the furnace which could pose an electrocution hazard.
3.2 Nitrogen gas line	Nitrogen canisters need to be properly hooked up to a regulator and into the retort controls of the furnace. Improper installation causes risks to equipment and could lead to a high pressure discharge of Nitrogen gas.
3.3 Furnace door operation	When the furnace is at high temperature, the door will become very hot. If touching the door is necessary, wear thick leather gloves.

B.4 Crucible Removal from Furnace

4.1 Power ramp down cycle	It is necessary to lower the temperature of the furnace to 550C prior to removing the crucibles. This is done to lower the temperature of the exterior of the furnace as well as to reduce the risk of thermal shock to any of the furnace components or crucibles while still maintaining the liquid state of the molten salt.
4.2 PPE	Two people are needed during the crucible removal process. Both should be wearing heat resistant gloves (ie, thick leather) as well as general shop required PPE (long pants, close toe shoes, safety glasses).
4.3 Partner assisted removal	One person will open the furnace door, while the other will be positioned so to remove one crucible at a time with the large tongs. Both persons need to be positioned so that their feet or appendages are not in a position of becoming burned or crushed by an accidental drop of the crucible.
4.4 Crucible cooling	After removal from the furnace, the crucibles should be placed to cool on heat resistant bricks and not near anything flammable. The crucibles should be left to cool overnight.

B.5 Crucible Opening

5.1 PPE	Personal protective equipment required by this step include general shop attire, thick leather gloves, a respirator mask, safety glasses and hearing protection. Respirator mask is worn to reduce inhalation of particulate matter and salt dust.
5.2 Tool preparation	Gather the required tools (vice and Metabo hand saw) and

	inspect for damage. Make sure the hand saw blade is not damaged as this could create high speed shrapnel upon breaking. If the blade is worn, replace.
5.3 Hand saw usage	Clamp the crucible in the vice and slowly saw around the circumference of the top in a uniform manner. Remove the sample rod gently with a pair of pliers.

B.6 Post Processing

6.1 Salt dry storage	Used salt needs to be put in dry atmosphere storage in dessecator of lab 914. Dessecator should be checked for any cracks which could result in structural damage during the vacuum process.
6.2 Sample cleaning	Sample coupons are to be ultrasonically cleaned in several different solvents (aluminum nitrate, ethanol and DI water). There is risk of splashing in the ultrasonic cleaning process so safety glasses should be worn or top places on ultrasonic device.